Trace element model studies of Nyanzian greenstone belts, western Kenya

PHILIP A. DAVIS, JR.* and KENT C. CONDIE

Department of Geoscience, New Mexico Institute of Mining and Technology,
Socorro, New Mexico 87801, U.S.A.

Abstract—The Archean greenstone belts of the Nyanzian System in western Kenya are composed principally of andesite with minor tholeiitic basalt and siliceous volcanics. The Nyanzian tholeiite is an intermediate-K tholeiite with a flat REE pattern. There are two chemically-distinct andesites: a low-K andesite (Andesite I) and a high-K andesite (Andesite II). The REE pattern of the Andesite II is enriched in light REE and depleted in heavy REE relative to Andesite I.

Major and trace element calculations indicate an origin for the Nyanzian tholeiite by 35–40% equilibrium melting of a lherzolite source followed by 10% shallow fractional crystallization. Similar calculations best explain Andesite I and Andesite II by 20 and 5% melting, respectively, of an ecologite or garnet amphibolite source of Nyanzian tholeiite composition. The rhyolite may have formed either by 20–30% partial melting of a siliceous granulite or by 20–30% fractional crystallization of a granodiorite parent magma.

With respect to total exposure areas, the Nyanzian volcanics have significantly less tholeiite and more andesite and siliceous volcanics than other Archean greenstone belts. If these abundances are representative, two models are proposed to explain the anomalous abundances of andesite and siliceous volcanics. The first model involves an Archaen upper mantle with a relatively low geothermal gradient beneath Kenya, while the second model involves a relatively cool mantle plume. Both models inhibit ascent of a significant amount of primary tholeiite to the surface and prevent formation of secondary tholeiite. Other Archean greenstone terranes with higher mantle geotherms or hotter mantle plumes would receive higher proportions of mafic and ultramafic magmas.

INTRODUCTION

THERE are two or possibly three greenstone belts exposed in western Kenya along the eastern border of Lake Victoria (Fig. 1). The largest exposure of greenstone terrane in this region is located north of the Kavirondian Gulf. This exposure strikes NE–SW and has a length of 85 km and a width of 65 km. South of the Kavirondian Gulf it is difficult to determine from the exposures whether the greenstone successions represent one NW–SE trending belt or two parallel belts. One of the parallel belts may be represented by the greenstone succession between the granite exposure southwest of Kisii and the Kavirondian Gulf. This sequence is exposed over an area of 40 × 40 km. The other belt may be delineated by the greenstone sequence located southwest of the previously mentioned granite exposure. This greenstone terrane is exposed for a length of 80 km and a width of 40 km. In northern Tanzania, remnants of greenstone successions occur as scattered exposures within a granitic gneiss complex, changing from an E–W strike along the eastern border of Lake Victoria to a NW–SE strike south of the lake.

In most of the Kenyan greenstone successions, the Nyanzian System is composed of tholeiitic basalt, andesite and siliceous volcanics in order of the oldest to youngest (HUDDLESTON, 1951; SAGGERSON, 1952).

PULFREY (1946), however, interpreted the reverse order for the Kisii and Kisumu districts. The greenstone belts are bordered on the east by younger Precambrian volcanics (mafic to siliceous) of the Bukoban System and on the west by Tertiary lavas and pyroclastics. Granitic gneiss of Archean age forms the southern boundary of the belts. The Nyanzian System is overlain unconformably by the Kavirondian System which is composed chiefly of conglomerate and subordinate arkosic grits (McCALL, 1958). Recent Rb–Sr age determinations of the basal Kavirondian conglomerate give a minimum age for the Nyanzian System of 2.8 ± 0.12 b.y. (DODSON et al., 1975).

With the exception of an extensive exposure north of the Kavirondian Gulf, the tholeiite outcrops are sparse and scattered (Fig. 1). The tholeiites are for the most part, pillowed and associated with minor but widespread chert, fine-grained tuff, and banded ironstone (HUDDLESTON, 1951; SAGGERSON, 1952). The andesites are concentrated mostly in the Kisumu and Sare districts with only subordinate, lenticular bands of little lateral extent in the Kisii district (HUDDLESTON, 1951; SAGGERSON, 1952). Tuffs and agglomerates are assoicated with the andesites in the Kisumu and Sare districts (HUDDLESTON, 1951). The andesites may be near-surface intrusions with minor, marginal extrusive phases near Sare and Nyagongo (McCALL, 1958). The largest exposure of the siliceous volcanics found in the Kisii district may also be a near-surface intrusion (McCALL, 1958). The siliceous volcanics contain small lenticular bodies of tuff and agglomerate

---

* Present address: Department of Geology, University of Kentucky, Lexington, Kentucky 40506, U.S.A.
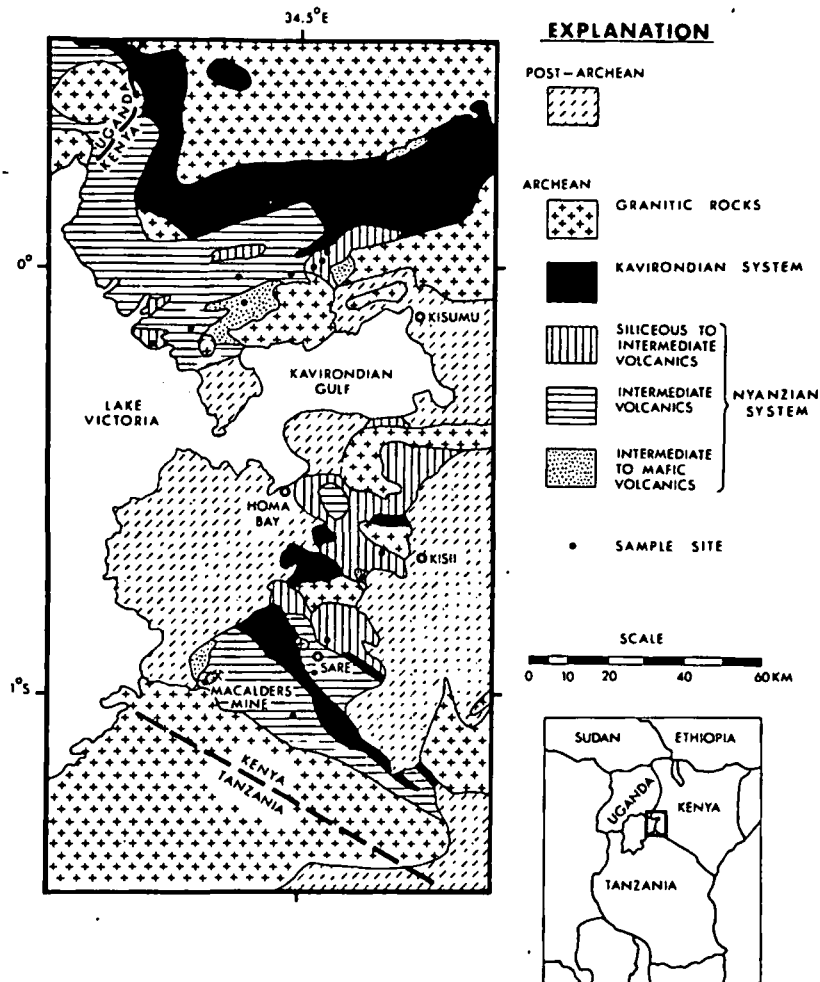
Fig. 1. Geological sketch map of Nyanzian greenstone belts, western Kenya (after HUDDLESTON, 1951; SAGGERSON, 1952; McCALL, 1958).

(SAGGERSON, 1952) and locally, banded ironstone (HUDDLESTON, 1951).

The metamorphic grade of the rocks in the Nyanzian System is predominantly greenschist. The degree of alteration varies from slight, towards outcrop centers, to intense near granitic contacts where rocks are sheared (HUDDLESTON, 1951; SAGGERSON, 1952). Away from outcrop margins the Nyanzian rocks contain primary structures and textures (pillows; relict phenocrysts of plagioclase and clinopyroxene; vesicles, and varioles) and lack foliation. Sample sites were chosen where weathering and metamorphic effects were at a minimum.

Fourteen samples were analyzed for major elements and 16 trace elements by X-ray fluorescence and neutron activation. The methods by which the analyses were performed are described elsewhere: major elements, except Na, CONDIE (1967); Na, Cr, and Co, STUEBER and GOLES (1967); REE, Ba, and Cs, GORDON et al. (1968); and Rb, Sr, Ni, Y, and Zr, REYNOLDS (1963). Most trace elements were determined using AGV-1 as the standard. W-1 was used for Y and Zr and JB-1 for Ni. Total analytical error

is estimated as follows: Major elements $\leq 3\%$ (Mg ~ 7 percent); REE, Co, Zr and Rb ~ 5–10%, except Tb $\sim 20\%$; Sr, Ba, Cr, Y, and Ni $\sim 10\%$; and Cs ~ 10–15%. The results are summarized in Table 1 in terms of averages.

RESULTS

Tholeiite

The composition of the one tholeiite sample found from all the samples analyzed from the Nyanzian greenstone belts is given in Table 1 together with the average composition of the Mafic Formation tholeiite of the Midlands greenstone belt, Rhodesia (CONDIE and HARRISON, 1976). The Nyanzian tholeiite (like the Mafic Formation tholeiite) is an intermedite-K tholeiite with a flat REE pattern (Fig. 2). Compositionally the only significant differences between the Nyanzian and the average Mafic Formation tholeiite are the higher K_2O, Rb, Cs, K/Ba and K/Rb ratios and lower Zr and to a lesser extent, light REE, in the Nyanzian tholeiite (Table 1). These higher concentrations of the large-ion lithophile (hereafter referred

Table 1. Average compositions of rocks from Archean greenstone belts in Kenya compared to average rock compositions from the Midlands greenstone belt, Rhodesia[1]

	Tholeiite		Andesite				Rhyolite	
	Kenya	Rhodesia[4]	Kenya		Rhodesia[4]		Kenya	Rhodesia[4]
		Mafic Fm.	I	II	Maliyami Fm.	Felsic Fm.		Midlands Belt
SiO2	49.1	50.5	56.9	56.8	56.6	59.7	75.3	71.7
TiO2	0.69	0.65	0.93	0.60	0.58	0.69	0.15	0.19
Al2O3	13.4	14.0	14.1	14.6	15.1	15.8	13.5	16.4
[2]Fe2O3	12.7	11.5	9.39	6.37	7.81	5.76	2.28	1.60
MgO	8.23	7.34	5.45	5.30	6.15	3.42	0.89	0.50
CaO	11.3	11.6	6.59	5.03	6.96	3.61	1.19	1.74
Na2O	1.68	2.05	3.37	3.22	2.86	5.46	3.46	5.00
K2O	0.29	0.06	0.79	2.60	0.85	1.62	3.53	2.05
[2]F/FM	0.61	0.61	0.63	0.54	0.56	0.63	0.72	0.76
CaO/Al2O3	0.84	0.84	0.47	0.34	0.46	0.23	0.09	0.11
Cr	410	338	154	102	74	54	-	9.7
Co	44	50	24	19	29	22	1.3	3.5
Ni	101	122	73	41	50	35	23	7
Rb	2.9	1.5	24	105	24	48	65	28
Sr	106	82	358	1164	241	291	23	100
Zr	45	100	177	224	75	65	357	30
Ba	104	110	237	999	228	310	954	330
Cs	1.4	0.53	1.0	2.4	0.90	1.2	0.14	0.87
La	3.0	4.3	15	39	10	26	64	18
Ce	5.6	10	34	92	24	50	146	34
Sm	1.6	2.3	4.4	7.5	2.7	5.1	15	1.9
Eu	0.67	0.68	1.2	2.3	1.1	1.5	2.4	0.47
Tb	0.43	0.56	0.62	1.4	0.53	0.57	-	0.17
Yb	1.6	2.4	1.9	1.0	1.3	1.6	9.9	0.28
Lu	0.37	0.40	0.34	0.18	0.20	0.24	1.6	0.04
Y	17	20	26	35	15	13	84	2
K/Ba	23	4.5	28	22	31	52	31	50
K/Rb	830	332	273	206	238	268	451	600
Rb/Sr	0.03	0.02	0.07	0.09	0.12	0.21	2.38	0.28
Ni/Co	2.3	2.4	3.0	2.2	1.7	1.6	17.1	210
La/Yb	1.9	1.8	7.6	38	7.7	16	6.5	64
[3]n	1		8	4			1	

[1] Major element concentrations are as measured with differences from 100% represented by volatiles.

[2] Total Fe as Fe2O3;

$$F/FM = \frac{Fe_2O_3}{Fe_2O_3 + M_sO}$$

[3] n = number of samples analyzed; individual sample compositions can be obtained from the senior author upon request.

[4] From CONDIE and HARRISON (1976).

LIL) elements (K, Rb, Sr, Cs, Ba) may be caused greater degree of alteration in the Nyanzian tholeiite. Extending this comparison to other Archean tholeiites (CONDIE and HARRISON, 1976), the same differences are noted with exception of K2O and Rb. Compared to modern tholeiites, the Nyanzian tholeiite is similar to arc and rise tholeiites in the flat REE pattern and overall chemical composition. It differs from arc tholeiites, however, by its low Al2O3,

Fig. 2. Average chondrite-normalized REE distributions in volcanic rocks of Nyanzian greenstone belts. Chondrite values from HASKIN et al. (1968).

Rb, Sr, Eu and K/Ba ratio and high Cr, Co, Ni, Ba and Cs and from rise tholeiites by its low Al2O3, TiO2, REE (except La and Lu) and K/B ratio and high Rb, Ba, Cs and Rb/Sr ratio (CONDIE and HARRISON, 1976). The higher Ba content and lower K/Ba ratio in the Nyanzian tholeiite is ascribed to Ba addition during alteration (PHILPOTTS et al., 1969). When plotted on the Ti–Zr–Y and Ti–Zr graphs of PEARCE and CANN (1973), the Nyanzian tholeiite falls in the field of arc tholeiites.

Andesites

The andesites of the Nyanzian System can be divided into two compositional groups: Andesite I and Andesite II. Andesite I is a low-K andesite and Andesite II a high-K andesite (latite andesite). The REE pattern of Andesite II is enriched in light REE and depleted in heavy REE relative to Andesite I (Fig. 2). It also differs by its high LIL-element contents and low total iron and TiO2 (Table 1). The high concentrations of K2O, Rb, Sr and Cs in Andesite II may have resulted from enrichment during alteration and metamorphism. The Andesite I samples vary
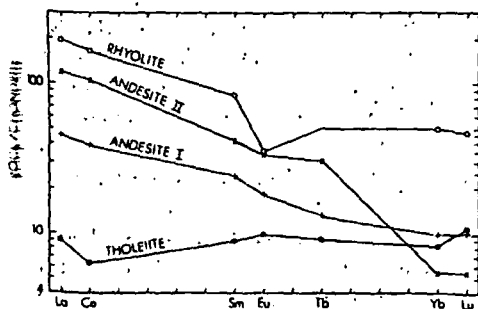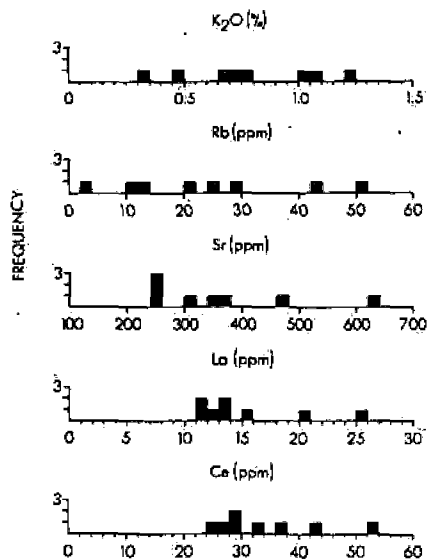
Fig. 3. Histograms showing variation of some LIL-element concentrations in Nyanzian Andesite I.

appreciably in their LIL-element concentrations. The variation appears to be random and is ascribed to varying amounts of sample alteration. Examples are shown in histogram form in Fig. 3 (La and Ce are included to show the variation in elements essentially unaffected by alteration and metamorphism, HERRMANN et al., 1974; GREEN et al., 1969). Cr and Ni concentrations also show variation in Andesite I samples. Both elements appear to increase with increasing amounts of clinopyroxene and magnetite in the samples.

Compared to other Archean andesites, Andesite I exhibits higher Y and Cr (Table 1). A striking similarity exists between Andesite I and the Coolgardie andesite of Western Australia (GLIKSON, 1970). This, however, is based solely on major element data. Andesite I is grossly similar to the andesites of the Maliyami Formation in the Midlands belt (CONDIE and HARRISON, 1976), but differs by having a slightly more enriched light REE pattern, more TiO_2, Zr and Y, a higher Ni/Co ratio and a lower Rb/Sr ratio (Table 1). In terms of modern andesites, the average composition and REE pattern of Andesite I is, for the most part, transitional between arc and calc-alkaline andesites. The term arc andesite used here refers to andesite of the 'island arc tholeiitic series' as defined by JAKES and GILL (1970). Andesite I differs from both of these groups, however, in its higher TiO_2, Cr, Ni, Zr and Ni/Co ratio and lower K/Ba and K/Rb ratios.

Compared to other Archean andesites, Andesite II is significantly higher in its LIL elements and La/Yb ratio (Table 1). Although Andesite II and the Felsic Formation andesites of the Midlands belt have REE patterns and major element concentrations that are quite similar (Fig. 2 and Table 1), their trace element compositions differ. In comparison to modern ande-

sites, Andesite II is most similar to high-K calc-alkaline andesites with respect to its enriched light REE pattern (Fig. 2), high Rb/Sr ratio, and high concentrations of LIL elements. Alteration in Andesite II may be responsible for the increased concentration levels of K_2O, Rb, Sr and Cs.

Rhyolite

The composition of the one rhyolite sample found from all the samples analyzed from the Nyanzian greenstone belts is given in Table 1 together with the average composition of the Midlands belt rhyolite. These two rhyolites have similar concentrations of some major elements, however, their trace element concentrations, element ratios and REE patterns differ (Fig. 2). Because of uncertainty in the Tb results, Tb was interpolated in the figure. Consequently, little significance can be assigned to the magnitude of the Eu anomaly. With regard to the average rhyolite from the Archean Canadian Shield (CONDIE and HARRISON, 1976), the chemical composition of the Nyanzian rhyolite differs for all elements except Ni.

In comparison to the average modern rhyolite (CONDIE and HARRISON, 1976), the Nyanzian rhyolite has more MgO, Ni, Y and REE, and higher K/Rb and Rb/Sr ratios, and less TiO_2, Co, Sr and Cs. The Nyanzian rhyolite is similar to modern rhyolites in that its REE pattern falls within the range of values for modern rhyolites.

DISCUSSION AND RESULTS

Origin for volcanic rocks of the Nyanzian System

has been appraised in terms of fractional crystallization and partial melting models with respect to both major and trace element data. Models were tested with major element concentrations using the methods of PEARCE (1968) and GILL (1974), and with trace element concentrations using the Rayleigh fractionation law and the partial melting equations derived by SHAW (1970). Compositions of the ultramafic source rocks and the distribution coefficients used in model calculations are given in Appendix I and II, respectively. Model calculations and comparisons involving the tholeiite and rhyolite depend upon their respective samples being representative.

Of all the partial melting and fractional crystallization models tested (see CONDIE and HARRISON, 1976, for the range of models tested) the Nyanzian tholeiite can best be explained by 35–40% melting of a lherzolite source with clinopyroxene (60%), olivine (30%) and orthopyroxene (10%) as solidus phases (relative proportions melted given in parentheses). The lherzolite model closely matches the Nyanzian tholeiite with respect to the REE, but is enriched by a factor of 2 in Cr, Co and Ni. The lower Cr, Co and Ni contents of the Nyanzian tholeiite relative to the lherzolite model is ascribed to these elements being trapped in residual chromite during partial melting or in sulfide phases during subsequent fractional crystallization.
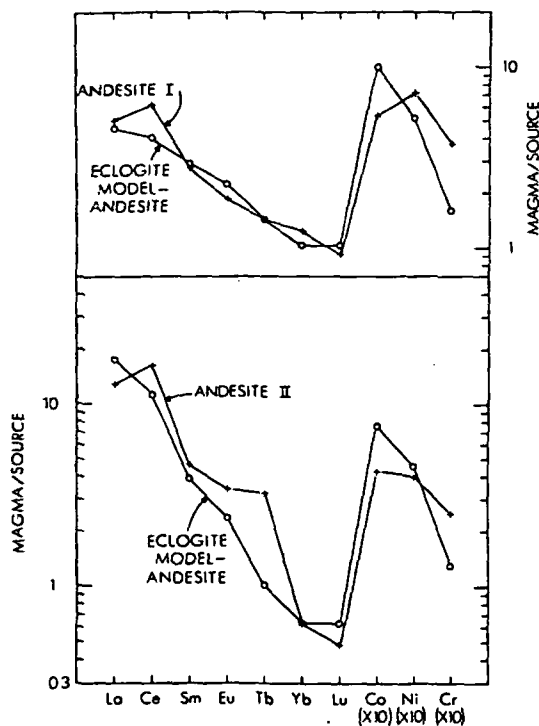
Fig. 4. Upper: eclogite-normalized trace element distributions in Andesite I compared to those of a model-andesite produced by 20% partial melting of eclogite with clinopyroxene (70%), garnet (10%) and quartz (20%) as solidus phases (relative proportions melted given in parentheses). Lower: eclogite-normalized trace element distributions in Andesite II compared to those of a model-andesite produced by 5% partial melting of eclogite with clinopyroxene (70%), garnet (20%), and quartz (10%) as solidus phases (relative proportions melted given in parentheses). Eclogite composition used in both andesite models was assumed to be that of the Nyanzian tholeiite. Distribution coefficients given in Appendix II.

The discrepancies are reduced by allowing 10% shallow fractional crystallization of olivine, clinopyroxene, and plagioclase ± magnetite or sulfide. This amount of fractional cyrstallization does not appreciably affect major or other trace element concentrations.

Fractional crystallization of the Nyanzian tholeiite was tested as a mechanism for the production of the andesites and rhyolite at various depth ranges using appropriate liquidus phases, but was unsuccessful. With the amounts of fractional crystallization given by the major element calculations, the model tholeiite has heavy REE values too low to produce the rhyolite or Andesite II trace element pattern and light REE values too low to produce the Andesite I trace element pattern. In terms of partial melting, neither a lherzolite nor a garnet or plagioclase peridotite is capable of producing the andesites or rhyolite. These model magmas are too low in the light REE and too high in the heavy REE values for the andesites, and are too in all REE values for the rhyolite. The model which is most acceptable for the Nyanzian andesites involves decreasing amounts of equilibrium

melting (from 20 to 5%) of an eclogite or garnet amphibolite source of Nyanzian tholeiite composition. The trace element patterns of Andesite I and Andesite II can be produced by approximately 20 and 5% melting, respectively, of such an eclogite (Fig. 4). Unlike the tholeiite, the andesites have a higher Cr content relative to the model magma. This suggests the presence of a crystallizing phase in the andesites which had a higher distribution coefficient for Cr relative to Co and Ni.

The trace element pattern of the Nyanzian rhyolite cannot be produced by partial melting of eclogite, garnet amphibolite, garnet granulite, or of an ultramafic rock because all the REE values of these magmas are much lower than those of the rhyolite. The models which most closely approach the trace element pattern of the rhyolite involve 20–30% equilibrium melting of a siliceous granulite or 20–30% fractional crystallization of a granodiorite parent magma. Neither model, however, can account for the high Yb and Lu and low Rb, Sr, Co and Ni values observed in the rhyolite.

Based on total apparent exposure area, the Nyanzian volcanics consist of significantly less tholeiite, and more andesite and siliceous volcanics than any other Archean greenstone terrane. This dissimilarity may be the result of selective exposure caused by a smaller degree of uplift and erosion. If, however, the observed distribution of rock types is representative, the Nyanzian volcanics must have formed under mantle conditions different from those of other Archean greenstone rocks. Two models are proposed for the origin of the Nyanzian volcanics in order to explain the anomalous abundance of andesites and siliceous volcanics.

The first model involves an Archean upper mantle with a lower geothermal gradient beneath Kenya than beneath other greenstone terranes. The lower geothermal gradient is envisaged as being similar to Green's geotherm II (GREEN, 1975). A lherzolite-derived, tholeiite magma rises to the lithosphere and lower crust and begins to cool. A small fraction of the magma reaches the surface while the remainder is intruded at depth and transforms to eclogite. Gravitationally unstable, the eclogite sinks into the upper mantle and partially melts. The mantle geothermal gradient, too low to initiate tholeiite magmatism, produces andesitic magmas. Since the solidus of peridotite is very similar to that of eclogite (HOWELLS et al., 1975), it is possible that peridotite may also partially melt under these conditions. However, the peridotite was unable to produce the andesites in the trace element modelling and is, therefore, excluded from this and the following model. In response to these ascending magmas, granodioritic crust partially melts and rises to a shallow depth where it fractionally crystallizes to produce rhyolite. A low Archean mantle geotherm beneath Kenya may have inhibited ascent of a significant amount of primary tholeiite to the surface and also prevented production of secondary tholeiite (i.e

tholeiite produced by the partial melting of eclogite or other mafic parent rock). On the other hand, other greenstone terranes with higher mantle geotherms would receive a greater proportion of mafic and ultramafic magmas.

The second model calls upon a mantle plume to explain the anomalous abundances in the Nyanzian System. A relatively cool rising mantle plume encounters and partially melts an eclogite layer at the base of the crust, resulting in the production of andesite magmas. The low temperature of the plume prevents formation of secondary tholeiite. The melting process further reduces the plume's temperature so that only a small fraction of the initial tholeiitic magma reaches the surface. The ascent of andesite magma through the crust produces rhyolite as in the first model. Most other Archean greenstone terranes may have had much hotter and larger plumes beneath them.

REFERENCES

CONDIE K. C. (1967) Petrology of the Precambrian tillite association in northern Utah. *Bull. Geol. Soc. Amer.* **78,** 1317–1338.

CONDIE K. C. and HARRISON N. M. (1976) Geochemistry of the Archean Bulawayan Group, Midlands greenstone belt, Rhodesia. *Precambrian Res.* **3,** 253–271.

CULLERS R. L., MEDARIS L. G. and HASKIN L. A. (1973) Experimental studies of the distribution of rare earths as trace elements among silicate minerals and liquids and water. *Geochim. Cosmochim. Acta* **37,** 1499–1512.

DODSON M. H., GLEDHILL A. R., SHACKLETON R. M. and BELL K. (1975) Age differences between Archean cratons of eastern and southern Africa. *Nature* **254,** 315–318.

GILL J. B. (1974) Role of underthrust oceanic crust in the genesis of a Fijian calcalkaline suite. *Contrib. Mineral. Petrol.* **43,** 29–45.

GLIKSON A. Y. (1970) Geosynclinal evolution and geochemical affinities of early Precambrian systems. *Tectonophysics* **9,** 397–433.

GORDON E. E., RANDLE K., GOLES G. G., CORLIS J. B., BEESON M. H. and OXLEY S. S. (1968) Instrument activation analysis of standard rocks with high resolution gama-ray detectors. *Geochim. Cosmochim. Acta* **32,** 369–396.

GREEN D. H. (1975) Genesis of Archean peridotitic magmas and constraints on Archean geothermal gradients and tectonics. *Geology* **3,** 15–18.

GREEN T. H., BRUNFELT A. O. and HEIER K. S. (1969) Rare earth element distribution in anorthosites and associated high grade metamorphic rocks, Lofoten–Vesteraalen, Norway. *Earth Planet. Sci. Lett.* **7,** 93–98.

HASKIN L. A., HASKIN M. A., FREY F. A. and WILDEMAN T. R. (1968) Relative and absolute terrestrial abundances of the rare earths. In *Origin and Distribution of the Elements,* (editor L. H. Ahrens), pp. 889–912. Pergamon Press.

HERRMANN A. G., POTTS M. J. and KNAKE D. (1974) Geochemistry of the rare earth elements in spilites from the oceanic and continental crust. *Contrib. Mineral. Petrol.* **44,** 1–16.

HIGUCHI H. and NAGASAWA H. (1969) Partition of trace elements between rock-forming minerals and the host volcanic rocks. *Earth Planet. Sci. Lett.* **7,** 281–287.

HOWELLS S., BEGG C. and O'HARA M. J. (1975) Crystallization of some natural eclogites and garnetiferous ultrabasic rocks at high pressure and temperature. In *Physics and Chemistry of the Earth,* (editors L. H. Ahrens, J. B. Dawson, A. R. Duncan and A. J. Erlank), Vol. 9, pp. 895–902. Pergamon Press.

HUDDLESTON A. (1951) Geology of the Kisii district, Kenya. *Geol. Surv. Kenya Rep.* **18,** 64 pp.

JAKES P. and GILL J. (1970) Rare earth elements and the island arc tholeiitic series. *Earth Planet. Sci. Lett.* **9,** 17–28.

McCALL G. J. H. (1958) Geology of the Gwasi area. *Geol. Surv. Kenya Rep.* **45,** 88 pp.

PEARCE J. A. and CANN J. R. (1973) Tectonic setting of basic volcanic rocks determined using trace element analyses. *Earth Planet. Sci. Lett.* **19,** 290–300.

PEARCE T. H. (1968) A contribution to the theory of variation diagrams. *Contrib. Mineral. Petrol.* **19,** 142–157.

PHILPOTTS J. A., SCHNETZLER C. C. and HART S. R. (1960) Submarine basalts: some K, Rb, Sr, Ba, rare-earth, H_2O, and CO_2 data bearing on their alteration, modification by plagioclase, and possible source materials. *Earth Planet. Sci. Lett.* **7,** 293–299.

PULFERY W. (1946) Geological survey of Maragoli, North Kavirondo. *Geol. Surv. Kenya Rep.* **9.**

REYNOLDS R. C., JR. (1963) Matrix corrections in trace element analysis by X-ray fluorescence: estimation of the mass absorption coefficient by Compton scattering. *Amer. Mineral.* **48,** 1133–1143.

SAGGERSON E. P. (1952) Geology of Kisumu district. *Geol. Surv. Kenya Rep.* **21,** 86 pp.

SCHNETZLER C. C. and PHILPOTTS J. A. (1970) Partition coefficients of rare-earth elements between igneous matrix material and rock-forming phenocrysts—II. *Geochim. Cosmochim. Acta* **34,** 331–340.

SHAW D. M. (1970) Trace element fractionation during anatexis. *Geochim. Cosmochim. Acta* **34,** 237–243.

STUEBER A. M. and GOLES G. G. (1967) Abundances of Na, Mn, Cr, Sc and Co in ultramafic rocks. *Geochim. Cosmochim. Acta* **31,** 75–93.

APPENDIX I

Trace-element composition (in ppm) of ultramafic source rocks used in model calculations

	Lherzolite and garnet peridotite	Plagioclase peridotite
La	1.3	3
Ce	3.5	6
Sm	0.75	1
Eu	0.28	0.30
Tb	0.19	0.30
Yb	0.75	0.75
Lu	0.15	0.15
Co	200	125
Cr	3400	3000
Ni	2500	2200

APPENDIX II

Solid/liquid distribution coefficients used in model calculation

	Olivine	Clinopyroxene	Orthopyroxene	Garnet	Amphibole	Plagioclase	Biotite	K-Feldspar	Magnetite
La	0.01	0.05 (0.3)	0.03 (0.1)	0.01 (0.1)	0.2 (1)	0.1 (0.3)	(0.3)	(0.05)	0
Ce	0.01	0.1 (0.5)	0.05 (0.2)	0.01 (0.3)	0.2 (2)	0.1 (0.3)	(0.3)	(0.05)	0
Sm	0.01	0.2 (0.6)	0.05 (0.2)	0.5 (3)	0.5 (7)	0.1 (0.15)	(0.3)	(0.05)	0
Eu	0.01	0.3 (1)	0.05 (0.15)	1 (3)	0.6 (5)	0.6 (1)	(0.25)	(1)	0
Tb	0.015	0.3 (1.5)	0.08 (0.3)	4 (15)	0.5 (6)	0.1 (0.05)	(0.3)	(0.03)	0
Yb	0.02	0.3 (2)	0.10 (0.8)	7 (25)	0.4 (5)	0.1 (0.05)	(0.4)	(0.01)	0
Lu	0.02	0.3 (2)	0.10 (0.8)	7 (25)	0.4 (5)	0.1 (0.05)	(0.4)	(0.01)	0
Co	6	1 (7)	3 (10)	3 (15)	1 (30)	0 (0)	(15)	(0)	10
Ni	15	3 (20)	6 (10)	0.6 (15)	3 (30)	0 (0)	(15)	(0)	10
Cr	0.1	10	2	5	7	0 (0)			75

Principal references: SCHNETZLER and PHILPOTTS (1970), CULLERS *et al.* (1973), and HIGUCHI and NAGASAWA (1969).

Values in parentheses used in rhyolite calculations.

UNIVERSITY OF UTAH RESEARCH INSTITUTE

UURI

EARTH SCIENCE LABORATORY
420 CHIPETA WAY, SUITE 120
SALT LAKE CITY, UTAH 84108
TELEPHONE 801-581-5283

July 17, 1980

Mr. P. Getecha
Technical Manager
Geothermal Exploration Project
The Kenya Power Company Limited
P. O. Box 49368
Nairobi, Kenya

Dear Mr. Getecha,

The effect of terrain on dipole-dipole resistivity data can be significant. A study of the topographic map and data from the Olkaria field, Kenya, shows that portions of some profiles are affected by the terrain but that most are not. The high resistivity surface layer is generally less than 250 m thick in the Olkaria area. In parts of the field, it may be too thin to affect our numerical models.

We have included a copy of our study 'Topographic Effects in Resistivity Surveys' which may help you appraise the shortcomings of flat-earth numerical models. Their advantage is that they are easier to interpret and less expensive to compute. Numerical models which include a topographic surface (e.g., Figures 1, 3, and 5) require twice the computation, time, and storage required by the standard flat-earth model, making routine use of topographic models impractical.

Our numerical models require the input of electrode locations. Terrain necessarily causes shortening of the actual dipole length, making electrode locations uncertain--the wire is still 250 m long, but the distance between its ends is less. Since electrode locations are the chief source of the observed topographic effect, it is critical that the locations be accurately known, if topographic effects are to be modeled. For example, an electrode at the base of a slope has a significantly different effect than an electrode on the slope. We do not know how accurately the electrode locations have been reproduced in the U. N. data package. This uncertainty makes topographic models of the Olkaria field suspect as well as expensive. The dipole lengths and electrode locations can be scaled from a map only for flat-earth models.

We have developed a two-part procedure for initiating a topographic modeling effort which we have implemented for portions of three profiles from Olkaria. First, we simulate the topography with a specifically designed mesh and assign to the "earth" a 100 ohm-meter resistivity and to the "air"

a 100,000 ohm-meter resistivity. The resulting model simulates a homogeneous earth with terrain below an infinitely resistive air. Figures 1, 3, and 5 are examples of this type of model that reveal the effects of topography on a homogeneous earth. Deviations from 100 ohm-meters in the calculated pseudosection represent topographic distortion. We make the assumption that similar deviations would occur over a nonhomogeneous two-dimensional earth.

The second step involves dividing the observed field data by the appropriate values computed by the homogeneous model with terrain. The result is a pseudosection 'corrected for topography,' Figures 2, 4, and 6. While it may not be rigorously correct, we assume that the values in the resulting pseudosection are the apparent resistivities that would have been observed were the terrain flat. Figures 2, 4, and 6 are, then, our approximations to the equivalent flat-earth case for the three profiles at Olkaria. The modeling would proceed with either flat-earth models matching the 'corrected' pseudosection or topographic models matching the observed pseudosection.

The topographic effects due to homogeneous earth models with terrain and their 'corrected' pseudosections have been calculated for the following profiles at Olkaria: Line 2 5/3 (page A-10 of 'Numerical Modeling and Interpretation of Dipole-dipole Resistivity Data, Olkaria Field, Kenya'), Line 10 W-Cntr (A-40), and Line 4 East (A-14). The terrain crossed by these lines produces moderate to strong topographic distortions. Profiles crossing similar terrain will suffer similar effects. If we had received the topographic map in the U. N. data package we would have attempted to incorporate it into our work, but additional costs would have been incurred. Most of the terrain at Olkaria is sufficiently gentle to justify the use of flat-earth models.

A line-by-line treatment follows a discussion of the effects of high resistivity surface layers on dipole-dipole data.

Topographic Effects at Olkaria, Kenya

Plate I of our report 'Numerical Modeling and Interpretation of Dipole-dipole Resistivity Data, Olkaria Field, Kenya' presents the interpreted intrinsic resistivity at the depth interval 150-250 m. High near-surface resistivities (greater than 400 ohm-meters) appear to the north, west, southwest, and southeast of the well field. These are areas where the resistive near-surface layers are sufficiently thick to affect the observed apparent resistivities at all depths. Plates 3-5 show the computed models. Most of the models contain thin resistive bodies at the surface, many of which are too thin to appear on Plate I. The thin, resistive surface bodies affect only the first few spacings in the pseudosections (N=2,3) and do not affect the deeper resistivity structure. In areas where our models do not contain resistive surface bodies, either the ground is conductive or the usually resistive ground is too thin to have an effect upon the resistivity pattern. Resistive surface layers less than 25 m thick will probably be transparent to the data.

We have compared the topographic map with Plates I and II to discern areas where there may be a positive correlation between topography and interpreted resistivity. Special attention has been paid to the well field northeast of the Ololbutot lava flow, Figures 1 and 2.

Several of the profiles cross valleys, ridges, or slopes. Lines 3, 4, 5, 6, and 8 cross the valleys north-northwest of the well field. Lines 5, 6, and 7 cross a valley northeast of the Olkaria volcano. A numerical model of the topography at the east end of Line 4 serves as an example of the effect that these valleys may have on the data, Figures 3 and 4. Ridges are crossed by Lines 9, 10, and 11 south of the Ololbutot flow and by Lines 4, 5, 6, and 7 north of the flow. The south end of Line 20 and the east end of Line 3 may be distorted by ridges as well. The center of Line 10, near Well Olk-1, is our example of the effect of a ridge, Figures 5 and 6. Line 18 descends a precipice south of the lava flow. Its slope length is 3 dipole lengths and its angle 20°. This is case S-SL 3.0-SA20 of Fox and others (1978), page A-59. These examples of homogeneous earth models are extreme cases which reveal the complexity of the topographic effect in areas with cliffs.

The well field appears to occupy a local depression that produces its strongest effect near the surface, Figure 1. The 56 ohm-meter value adjacent to the 134 ohm-meter east of Station 15, Line 2, presents the greatest contrast in the area. The observed data for this area are shown on Plate III of our report. At the same locations, the observed apparent resistivities are 7 and 42 ohm-meters, respectively and our calculated model contains many small resistive bodies. When the topographic effect is divided into the observed data, the reduced apparent resistivities are 12 and 31 ohm-meters, Figure 2, a contrast of 2½ rather than 6. It would be simpler to produce a satisfactory fit to the reduced rather than the raw data. It would also be simpler to match the raw data using the mesh of Figure 1 than it was with the flat earth mesh, page A-10. We could compute these models in detail only if funding were made available and the schedule of other work permitted.

The reduced pseudosection would not require the complexity of the flat-earth model. While details would change, both the 5 and 60 ohm-meter bodies can be expected to remain. The near-surface resistivity is low (5 ohm-meters) between Stations 13 and 16. The 20,000 ohm-meter value at the east end of Line 2 may be spurious (bad data?) or due to a local 3D anomaly.

The most prominent correlation with a ridge is the north-south trend of high resistivities south of the Ololbutot lava flow near Well Olk-1, Lines 9, 10, and 11. These profiles cross a topographic spur with more than 60 m of elevation change over a distance of 500 m, two dipole lengths. Figure 3 is our numerical model for the center of Line 10. The topography produces both artificially high and low apparent resistivities--high below the crest of the ridge and low at the base of its slopes. The greatest distortion occurs at N=3 below Station 5.

A comparison of the observed data, Plate V, and the topography-corrected pseudosection, Figure 4, reveals that the symmetrical bands of high resistivity on the diagonals below Stations 4-6 are better developed in the reduced data.

These bands require a highly resistive near-surface body between these stations--the ridge is resistive. Several iterations with the mesh of Figure 3 would be necessary to determine the depth to the top of the 50 ohm-meter body below the ridge, Plate V. It is possible that the conductive bodies shown flanking the ridge are continuous below it. If so, the resistive pattern shown in Plate I may be suspect.

Line 4 East crosses both a ridge and a valley, perhaps the most severe terrain in the data package. The topographic effects in Figure 5 have the same pattern as the observed values in Plate III--low resistivities below the valley and high below the ridge. When the topographic effect is divided into to raw data, the resistivities increase below the valley and decrease below the ridge but the pattern remains virtually unchanged. A simulation of Line 4 East with the mesh of Figure 5 would require the same type of resistivity distribution as the flat-earth model. Three-dimensional structures are likely between Stations 4 and 5E. The topographic map reveals that a pipeline passes between these two stations. What effect the pipeline has on the apparent resistivities of (the parallel) Line 2 are unknown. It should be noted that we required 19 iterations to produce the flat-earth model for Line 4 East, page A-14. This is an uncommonly high number of iterations. The topographic model might produce a more satisfactory match with less effort.

We thank you for your patience and your interest in future co-operation. The Earth Science Laboratory would like to keep appraised of geothermal development in Kenya. I hope you find these comments useful in your evaluation of the resistivity data.
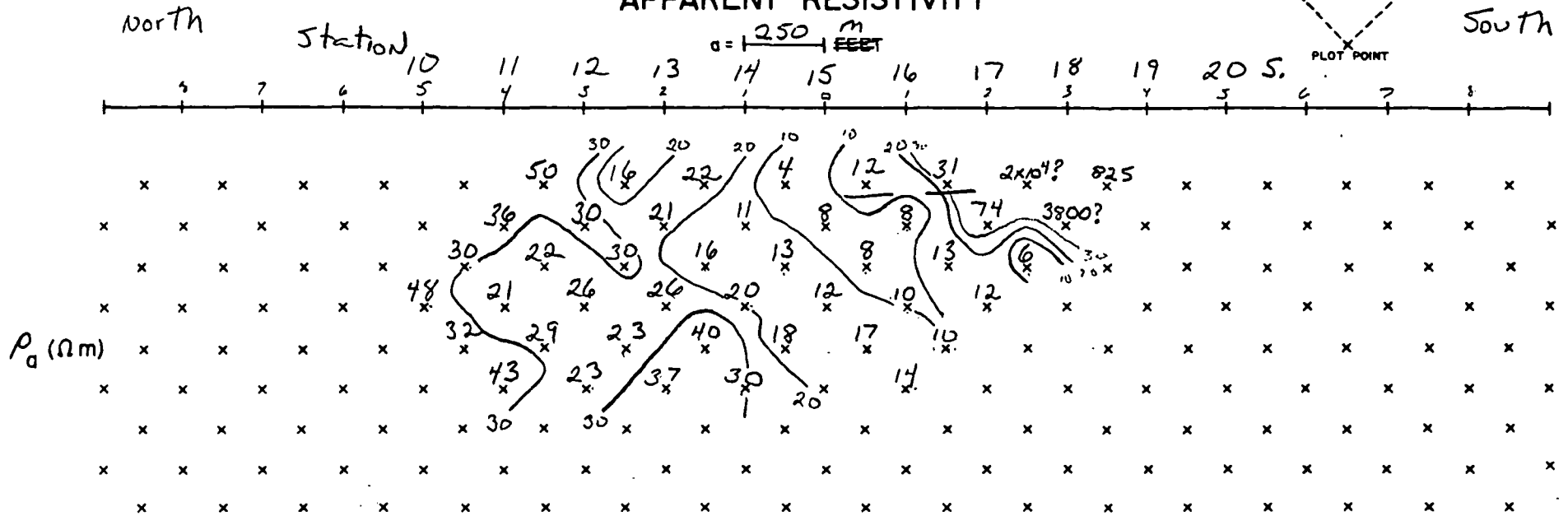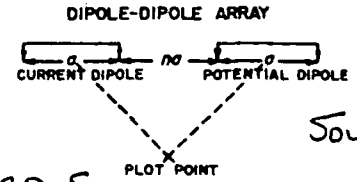
Sincerely,

Christian Smith by HPR

Christian Smith
Associate Geophysicist

CS/pf
cc: Mr. H. P. Ross

OLKARIA KENYA TOPOGRAPHY TEST   Figure 1
LINE 2 S/3 (A 10)
MEDIA RESITIVITY (OHM-METERS)
        0.00   1 dipole length = a = 250 m
MEDIA PFE (%)   well Field
North   0.00   10   15   20 station   South thickness
        8   7   6   5   4   3   2   1   0   1   2   3   4   5   6   7   8   (a)
....|....|...1.|....|....|2....|....|....|.3.|....|....|4....|....|....|5....|....|....|6....|....|....|.7

22222222222222222220001111111111111111111111111111111111111111111111111111   .1
2222222222222222222222220111111111111111111111111111111111111111111111111111   .1
2222222222222222222222222220111111111111111111111111111111111111111111111111   .1
2222222222222222222222222222222220111111111110220111111111111111111111111   .1
222222222222222222222222222222222222220110222200222220111111111111111111111   .1
2222222222222222222222222222222222222222222222222222222220111111111111111111   .1
222222222222222222222222222222222222222222222222222222222220111111111111111   .1
22222222222222222222222222222222222222222222222222222222222222222222222222   .1
22222222222222222222222222222222222222222222222222222222222222222222222222   .2
22222222222222222222222222222222222222222222222222222222222222222222222222   .3
22222222222222222222222222222222222222222222222222222222222222222222222222   .4
22222222222222222222222222222222222222222222222222222222222222222222222222   .5
22222222222222222222222222222222222222222222222222222222222222222222222222   .5
22222222222222222222222222222222222222222222222222222222222222222222222222   1.
22222222222222222222222222222222222222222222222222222222222222222222222222   2.
22222222222222222222222222222222222222222222222222222222222222222222222222   8.
.........1.........2.........3.........4.........5.........6.........7

CALCULATED RESISTIVITY (OHM-METERS) ohm-m   Station
    10   15   20
    -5   -4   -3   -2   -1   0   +1   +2   +3   +4   +5
    :------:------:------:------:------:------:------:------:------:------:

N= 2   103.   77.   94.   120.   56.   134.   70.   114.   Limit of detn

  = 3   117.   90.   77.   131.   77.   87.   102.   97.   115.

  = 4   119.   103.   82.   108.   85.   105.   68.   136.   97.   107.

  = 5 120.   106.   92.   113.   71.   113.   80.   90.   138.   90.   106.

  = 6 108.   94.   126.   73.   93.   86.   105.   93.   130.   88.

  = 7   95.   129.   82.   94.   111.   108.   88.   127.

CALCULATED PFE (%)

    -5   -4   -3   -2   -1   0   +1   +2   +3   +4   +5
    :------:------:------:------:------:------:------:------:------:------:

            0.00   0.00   0.00   0.00   0.00   0.00   0.00   0.00

        0.00   0.00   0.00   0.00   0.00   0.00   0.00   0.00   0.00

    0.00   0.00   0.00   0.00   0.00   0.00   0.00   0.00   0.00   0.00

Figure 2

EARTH SCIENCE LABORATORY
UNIVERSITY of UTAH RESEARCH INSTITUTE
DIPOLE – DIPOLE ARRAY
APPARENT RESISTIVITY

Observed Apparent Resistivity corrected for Topography
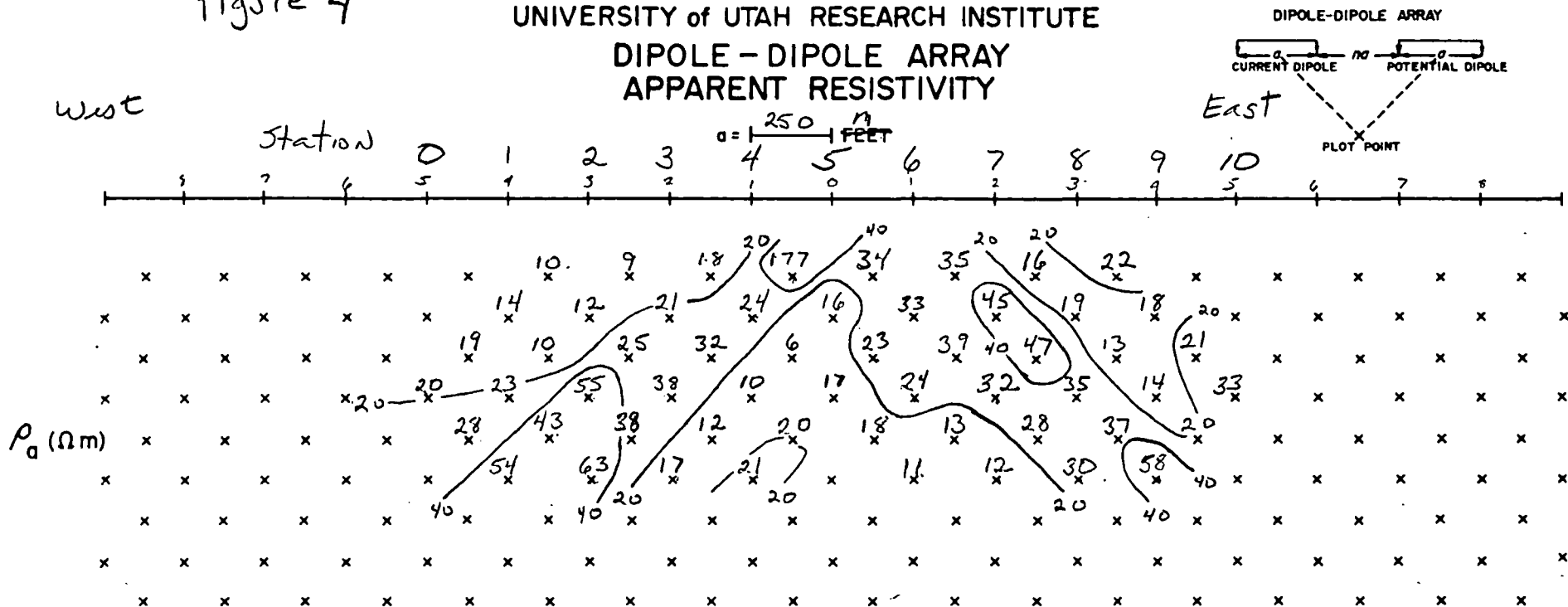
Line 2 $\frac{S}{3}$

AREA _Olkaria Kenya_ STATE_____ LINE $2 \frac{S}{3}$ DATA BY_____ DATE_____ TRANSMITTER_____ RECEIVER_____

KIP

Figure 3

OLKARIA KENYA TOPOGRAPHY TEST
LINE 10 W-CNTR   (A 40)
MEDIA RESITIVITY (OHM-METERS)
    100000.00   100.00
MEDIA PFE (%)
West   0.00   0.00   4 5 6 - Stations -10   East   thickness
       8   7   6   5   4   3   2   1   0   1   2   3   4   5   6   7   8   (a)
...|...|..1.|....|....|2...|...|..3.|...|...|4...|...|...|5.|...|...|6..|...|...|.7
1111111111111111111111111111111111111110201111111111111111111111111111111111111 .1
1111111111111111111111111111111111111110222011111111111111111111111111111111111 .1
22222220111111111111111111111111110222222220111110222222011111111111111111111 .1
222222222011111111111111111111111102222222222222222222222222222220111111111111 .1
2222222222220111111111111111111102222222222222222222222222222222200222222222 .1
22222222222222200022222222222222222222222222222222222222222222222222222222222 .1
22222222222222222222222222222222222222222222222222222222222222222222222222222 .1
22222222222222222222222222222222222222222222222222222222222222222222222222222 .2
22222222222222222222222222222222222222222222222222222222222222222222222222222 .3
22222222222222222222222222222222222222222222222222222222222222222222222222222 .4
22222222222222222222222222222222222222222222222222222222222222222222222222222 .5
22222222222222222222222222222222222222222222222222222222222222222222222222222 .5
22222222222222222222222222222222222222222222222222222222222222222222222222222 1.
22222222222222222222222222222222222222222222222222222222222222222222222222222 2.
22222222222222222222222222222222222222222222222222222222222222222222222222222 8.
.........1.......2........3........4........5.........6........7

1 dipole length = a = 250 m

APPARENT RESISTIVITY (CALCULATED) ohm-m   Station

    0   4   5   6   10
   -5   -4   -3   -2   -1   0   +1   +2   +3   +4   +5
  : ------: ------: ------: ------: ------: ------: ------: ------: ------: ------:

N= 2   100.   102.   71.   88.   130.   69.   92.   106.

  = 3   102.   114.   77.   71.   153.   104.   65.   112.   104.

  = 4 91.   116.   84.   69.   121.   132.   90.   75.   110.   119.

  = 5 79.   103.   86.   72.   116.   109.   115.   100.   72.   128.   105.

  = 6 · 89.   76.   72.   121.   105.   96.   129.   95.   83.   113.

  = 7   65.   63.   120.   110.   109.   124.   109.   74.

Figure 4

EARTH SCIENCE LABORATORY
UNIVERSITY of UTAH RESEARCH INSTITUTE
DIPOLE – DIPOLE ARRAY
APPARENT RESISTIVITY

Observed Apparent Resistivity corrected For Topography

LINE 10 W-Cntr

AREA Olkaria Kenya ___ STATE ___ LINE 10 W-Cntr DATA BY ___ DATE ___ TRANSMITTER ___ RECEIVER ___

KIP

MEDIA RESITIVITY (OHM-METERS)
   100000.00   100.00

1 dipole length = a = 250m

MEDIA PFE (%)

West   0.00 2W 0.00 0   3 4 5 — stations — 8E   East

```
        6   7   6   5   4   3   2   3 1   0   |4   2   3   5 4   5   6   7   7        Thickness
 .....:...:...1.1........:..2...:...3.:..:...|4...:...:..5.:....:...:6..:...:...7      (a)
1111111111111111111111111111111111100111111111111111111111111022222222222222 ,1
1111111111111111111111111111111110222222011111111111111111111022222222222222 ,1
1111111111111111111111111111110222222222201111111111111111102222222222222222 ,1
1111111111111111111111111110222222222222201111111111111102222222222222222222 ,1
1111111111111111111111110222222222222222201111111111110222222222222222222222 ,1
1111111111111111111102222222222222222222222011111111022222222222222222222222 ,1
222222222222222222222222222222222222222222201111102222222222222222222222222 ,1
22222222222222222222222222222222222222222222222222222222222222222222222222 ,1
2222222222222222222222222222222222222222222222222222222222222222222222222222 ,2
2222222222222222222222222222222222222222222222222222222222222222222222222222 ,3
2222222222222222222222222222222222222222222222222222222222222222222222222222 ,4
2222222222222222222222222222222222222222222222222222222222222222222222222222 ,5
2222222222222222222222222222222222222222222222222222222222222222222222222222 ,5
2222222222222222222222222222222222222222222222222222222222222222222222222222 1.
2222222222222222222222222222222222222222222222222222222222222222222222222222 2.
2222222222222222222222222222222222222222222222222222222222222222222222222228 .
........1.........2.........3.........4.........5.........6.........7
```

                                                  Station

APPARENT RESISTIVITY (CALCULATED) ohm-m

2W   0   3E   4   5   8E

-5	-4	-3	-2	-1	0	+1	+2	+3	+4	+5
:——:	——:	——:	——:	——:	——:	——:	——:	——:	——:	——:

Limit of data

N= 2		96.	77.	102.	100.	104.	67.	106.	74.		
= 3	102.	82.	87.	120.	130.	80.	75.	86.	72.		
= 4	102.	83.	85.	102.	166.	100.	80.	59.	76.	98.	
= 5	102.	81.	83.	98.	148.	135.	98.	61.	49.	100.	110.
= 6	81.	80.	95.	146.	125.	133.	73.	49.	63.	111.	
= 7		78.	90.	143.	126.		98.	57.	61.	70.	

DIPOLE-DIPOLE ARRAY

CURRENT DIPOLE   POTENTIAL DIPOLE

PLOT POINT

West   2W   O   a = 250 m / FEET   3E   4   5   8E   East

8   7   6   5   4   3   2   1   0   1   2   3   4   5   6   7   8

$\rho_a\ (\Omega m)$

28 50 100   100 50
17   77   318   280   425   64   26   138
12   17   44   68   122   30   56   36   50
20   15   18   11   21   26   51   30   66   50
24   31   12   15   12   11   43   31   50
52   21   18   11   11   11   38
50   32   31   15   7   13   20
20
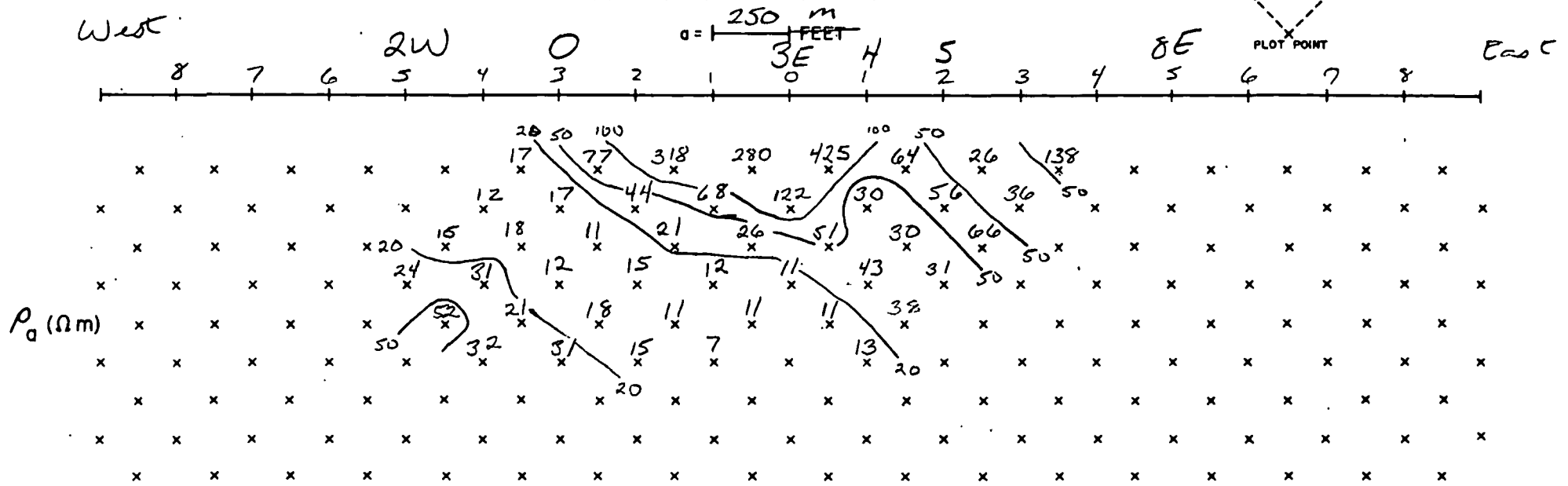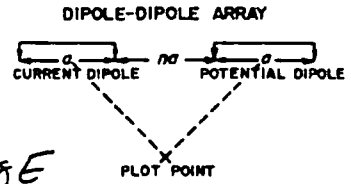
Observed Apparent Resistivity corrected For Topography

Line 4 East

UNIVERSITY OF UTAH RESEARCH INSTITUTE

UURI

EARTH SCIENCE LABORATORY
420 CHIPETA WAY, SUITE 120
SALT LAKE CITY, UTAH 84108
TELEPHONE 801-581-5283

July 17, 1980

Mr. P. Getecha
Technical Manager
Geothermal Exploration Project
The Kenya Power Company Limited
P. O. Box 49368
Nairobi, Kenya
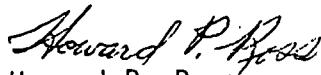
Dear Mr. Getecha,

Thank you for your letter of 23 June, 1980. I regret that through a breakdown of communications you were not aware of our receipt of your earlier letter dated 18 September, 1979. We received the topographic map in good order and gave brief consideration to the topographic problem at that time. It appeared that only minor topographic effects would be present and the cost of additional interpretation would be substantial. Since we were totally committed to other projects we did not consider it further.

Upon receipt of your letter of 23 June I asked my associate Mr. Christian Smith (who has become quite expert in the interpretation of topographic effects in resistivity data) to make a more detailed evaluation of the problem. As Mr. Smith points out, numerical modeling which incorporates a topographic surface is roughly twice as time consuming and expensive, and without additional funding we are limited in the additional interpretation we can do. Mr. Smith has tried to consider the most important areas in his new review and submits these results in an accompanying letter. We submit this information in the hope it will be of some help in your development of the geothermal field. We would appreciate learning more about the geothermal resources of this area, and your drilling results, when reports could be made available.

If you have additional specific questions concerning our interpretation please contact Mr. Smith or myself, and we will try to respond in a timely manner.

Sincerely,

Howard P. Ross
Senior Geophysicist

HR/pf
cc: Mr. C. Smith

The mapping of induced currents around the Kenya Rift: a comparison of techniques

D. Beamish *Department of Environment Sciences, University of Lancaster, Lancaster, LA1 4YQ*

Summary. Single-station and inter-station transfer functions are derived from data recorded by a magnetometer array in and around the Kenya Rift Valley. Different methods of presentation of the transfer function estimates are compared in terms of their ability to define lateral variations in electrical conductivity. When, as in East Africa, the conductivity structure is complex and three-dimensional, by far the most useful method of presentation is to use the transfer functions to simulate the anomalous internal fields associated with regional current flow at a particular azimuth. The use of inter-station rather than single-station transfer functions is almost essential where the amplitudes of anomalous horizontal fields are of the same size or greater than the normal fields. Horizontal field transfer functions prove to be just as useful as those usually calculated for the vertical component, and provide strong additional constraints on the internal current system.

Maps of simulated vertical and horizontal fields of internal origin indicate the importance of current channelling around the Rift Valley. A conductor just to the east of Nairobi apparently funnels regionally induced currents into two conductors associated with the Rift and dome; one at shallow depths beneath the Rift floor, and a deeper body to the east.

1 Introduction

The object of Geomagnetic Deep Sounding experiments, is to determine the distribution of electrical conductivity within the Earth from array measurements of magnetic field variations at the surface. The achievement of this objective essentially involves:

(1) The separation of the recorded magnetic field variations into parts of internal and external origin. The only viable approach so far developed is by the calculation of transfer functions (Schmucker 1970).

(2) The determination of the internal current system responsible for the internal component of the magnetic field variations. This is not an essential step since we could and do model the internal magnetic fields directly from proposed conductivity structures. However

Present address: Institute of Geological Sciences, Geomagnetism Unit, Murchison House, West Mains Road, Edinburgh, EH9 3LA.

it is only by forming a picture of the internal current system that reasonable constraints can be set on the class of conductivity structures whose responses will be modelled. The problem of determining the currents from the fields is of course non-unique; it is at this stage that other geological and geophysical constraints can be imposed.

(3) The inversion of the internal fields or currents determined in (1) and (2) to obtain the conductivity structure. Because of the limitations of computational time, only the forward problem is usually undertaken, and only two-dimensional structures can be considered as viable models.

This paper is concerned with stages (1) and (2) of the analysis. Data from a magnetometer array experiment in East Africa is used as a basis for the assessment of both old and new ways of mapping internal currents.

2 Experimental details

In 1972, 22 magnetometers of Gough—Reitzal type, were installed at sites in and around the Gregory Rift Valley in Kenya. The array experiment followed a pilot study, undertaken in 1971, for which six magnetometers were available. The results of the pilot experiment, across an east—west (E—W) equatorial profile, were interpreted in terms of two regions of high conductivity, one beneath the Rift floor at a depth of 20 km and a thicker/broader zone, 100 km to the east of the Rift axis, at a depth of about 50 km. The results are described in detail by Banks & Ottey (1974).

The large-scale experiment was designed to delineate the lateral extent of the anomalous zones and to provide data with a wide frequency content so as to obtain better bounds on the depths and thicknesses of the anomalous zones. On the basis of the lateral scales of the anomalies found in the pilot experiment the station spacing was limited to less than 50 km in the vicinity of the Rift and extended to 80 km to the west and east of the main Rift structure. The locations of the magnetometer stations are shown in Fig. 1. The diagram shows the main boundary faults of the graben which should be viewed as a simplified outline. The main Gregory Rift is shown striking approximately N—S with the minor Kavirondo Rift in the west striking E—W towards Lake Victoria. The stations KAB, MLO, NAK, TFL, NYK and MER were reoccupied from the 1971 experiment and together with HBY, KSI and NJO will be referred to as the equatorial line of stations.

The array was operational for three months during which time a variety of bay and substorm activity was recorded. A general feature of the low-latitude magnetic disturbances
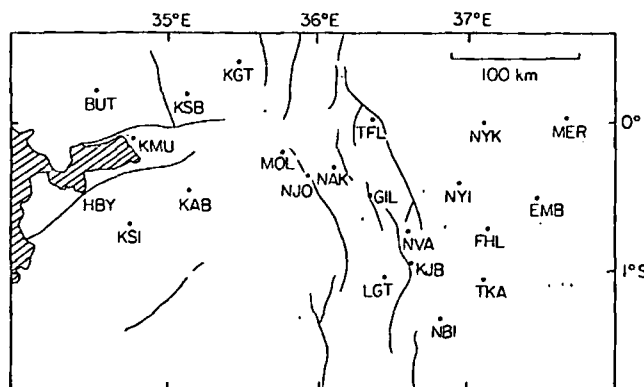
Figure 1. Location of the magnetometer stations relative to the main Rift faults.

was the low power levels; the bay fields recorded in. Kenya being several nT in the vertical component and less than 20 nT in the horizontal components. The basic instrumental sampling rate was 10 s. The raw photographic data containing activity with appreciable levels of power and a wide frequency content was subsequently digitized and data series sampled at 0.5- and 1-min intervals were obtained. Due to the low power levels of bay field activity, the majority of records were obtained from continuous storm/substorm disturbances. Record lengths ranged from 3 to 18 hr for individual disturbed periods of activity. Four to five such records were selected for each station and they form the basis of the subsequent analysis.

Displays of raw magnetograms are generally not very informative. Anomalies are typically frequency dependent so that the reader has to perform a mental Fourier Transform or filtering operation. A more direct way of showing the differences in the variation fields caused by anomalous structure at different stations is to present demodulated magnetograms. Complex demodulation as an alternative approach to the data processing of geomagnetic time-series has recently been studied by Banks (1975). The technique allows the variation with time of the amplitude and phase of selected frequency components of a data series to be examined. Following the basic formulation and computational scheme given by Banks (1975), the data under study was divided into bands of frequencies each central about a frequency of interest. For the continuous type of activity recorded in Kenya, spectral bands that varied linearly with period were chosen. Spectral bands containing Fourier components with periods 512–128, 128–64, 64–32, 32–16, 16–8 and 8–4 min were used throughout the analysis.

Fig. 2 shows a set of demodulates $|H_d|$, $|D_d|$ and $|Z_d|$ (H, D, Z are the normally defined geomagnetic axes) for three hours of substorm activity at 11 stations across the array for which simultaneous records are available. The original records are sampled at 0.5-min intervals and the demodulates shown are calculated for the period band $T = 32–16$ min. Banks & Ottey (1974) showed that the anomalous response is most pronounced within this band. The process of complex demodulation has isolated those variations in the period range 32–16 min contained within the original record while preserving their original local time. It is informative to consider the two main 'events' indicated by the demodulates with regard to anomalous behaviour across the array. The demodulates for the H component possess a consistent form across the array. The two exceptions are NYI and NYK which
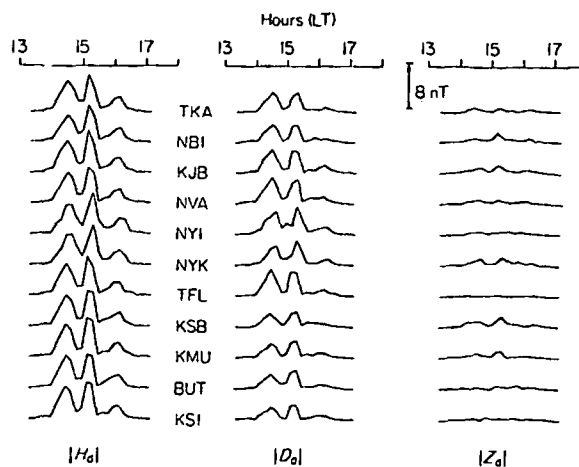
Figure 2. Simultaneous demodulated magnetograms in the period band $T = 32–16$ min for the substorm of 1972 September 14.

10

show a phase-lag with respect to the rest of the stations. There are slight variations in the magnitude of the two peaks, the most consistent magnitudes being produced at the western stations KSB, KMU, KSI and BUT. The corresponding events in the D component possess a greater degree of variability across the array, attributable to a proportionally larger anomalous internal component. The most striking feature is the consistency of $|D_d|$ at the western stations and the enhancement of $|D_d|$ at other stations with respect to these. Both events observed in the vertical field demodulates are clearly anomalous with little or no normal vertical field detectable across the array. The attenuation observed in $|Z_d|$ at TFL (on the eastern escarpment of the Rift) indicates that the station lies above a conductive structure. The vertical field demodulates at the extreme western stations KSI and BUT exhibit a similar form. When considered in conjunction with the absence of anomalous horizontal fields at the western stations it is reasonable to suppose that the extreme western stations are sufficiently far removed from the anomalous region that they record a predominantly normal variation field.

3 Transfer function methods

The first stage in the analysis of magnetometer array data is usually an attempt to separate the anomalous internal component of the recorded fields. Formal techniques do exist for performing internal/external field separations (Porath, Oldenburg & Gough 1970), but, in addition to involving a great deal of computational effort, they are unsatisfactory because assumptions must be made concerning the structure of fields with scale-lengths greater than the dimensions of the magnetometer array (Banks 1973). An alternative approach, that does not require large numbers of simultaneous measurements, or so much analysis, is to compute transfer functions between field components. If certain assumptions can be made, these transfer functions contain the required information concerning the nature of the internal fields across the array region. It is usual to compute transfer functions that relate the vertical and horizontal fields at a single station. Although these single-station transfer functions possess advantages, the underlying assumptions may not be valid and may lead to misleading conclusions. The data from the Kenya array is used to illustrate this point and to show the advantages gained using inter-station transfer functions.

3.1 SINGLE-STATION TRANSFER FUNCTIONS AND THE UNDERLYING ASSUMPTIONS

A consequence of the linearity of Maxwell's field equations is that we may assume that there exists a linear relationship between the Fourier transforms of the anomalous and normal field components. For fields measured at some point P, the relationships will take the form

$$H_a = T_{HH}H_n + T_{HD}D_n + T_{HZ}Z_n$$
$$D_a = T_{DH}H_n + T_{DD}D_n + T_{DZ}Z_n \tag{1}$$
$$Z_a = T_{ZH}H_n + T_{ZD}D_n + T_{ZZ}Z_n$$

at a particular frequency (Schmucker 1970). The subscripts a and n refer to anomalous and normal parts respectively. Omitting a dependence of each term on the wavelength of the source field in (1) is valid when the skin-depth of the source field is much less than its spatial wavelength. The transfer functions (the set of T's) should characterize the anomalous conductivity structure in the vicinity of point P. If the normal field (H_n, D_n, Z_n) is known then the observed fields (F) can be introduced using $F = F_a + F_n$, and the matrix of transfer

ight variations in the
duced at the western
component possess a
proportionally larger
stency of $|D_d|$ at the
espect to these. Both
us with little or no
ved in $|Z_d|$ at TFL
; above a conductive
itions KSI and BUT
sence of anomalous
the extreme western
they record a pre-

attempt to separate
hniques do exist for
ough 1970), but, in
satisfactory because
lengths greater than
approach, that does
alysis, is to compute
can be made, these
ture of the internal
at relate the vertical
transfer functions
y lead to misleading
int and to show the

YING

y assume that there
malous and normal
will take the form

(1)

cfer to anomalous
wavelength of the
less than its spatial
c the anomalous
. D_n, Z_n) is known
matrix of transfer

functions determined using cross-spectra calculated between the field components. Since there is, in practice, a great difficulty in the estimation of the normal field at each point within the array region, three simplifying assumptions can be introduced which, to a certain extent, allow this problem to be overcome (Banks 1973)

(1) That if Z_n is small compared with Z, then the terms T_{HZ}, T_{DZ} and T_{ZZ} in (1) can be ignored.

(2) That there is no correlation of Z_n with H_n and D_n.

(3) That both H_a and D_a are small in comparison to the total observed fields, in such circumstances H_n and D_n can be replaced by H and D (the observed fields) respectively.

If these assumptions are justified, the third equation of (1), characterizing the anomalous vertical field, reduces to

$$Z_c = AH + BD \tag{2}$$

at a particular frequency. Z_c is an estimate of Z_a whose validity depends on the validity of the above assumptions. The subscript c denotes that both A and B are defined using the vertical field that correlates with the right-hand side of (2) in a least-squares sense.

As far as the Kenya data is concerned, it is evident from Fig. 2 that the variation in the observed vertical field between stations is large and therefore predominantly anomalous; the wavelengths of the equatorial external fields being sufficiently large to produce a low-amplitude normal Z variation field. This effect was noted over a period range extending from 4 min to 24 hr. It is therefore considered that assumption (1) is well justified at the low latitudes of the Kenya array study. Persistent correlations between Z_n and H_n or D_n can only arise if the fields are generated by persistent external current systems. The only possible such correlation that might arise in East Africa is between Z_n and H_n, due to the equatorial electrojet. The fact that normal (i.e. western) stations show almost complete $Z-D_n$ correlations indicates that Z_n is too small for this effect to influence the estimates of the transfer functions. The demodulates of Fig. 2 indicate that assumption (3) is not valid for the data under consideration. The condition that $H_a \ll H$ is thought to be acceptable. However the predominant N–S directional nature of the magnetic field disturbances recorded at low latitudes (see below) result in a low-amplitude D_n variation field. The anomalous D component field may then form a substantial fraction of the observed D component field. Transfer functions calculated according to (2) will then be biased because assumption (3) is incorrect. A further possible complication arises because the magnetic field disturbances in Kenya tend to be polarized in a N–S direction. Banks (1975) has shown that the transfer functions derived from such data will not be biased, but the errors in the transfer functions relating anomalous field components to the D variation field will be large.

Given that assumptions (1) and (3) are valid for a particular array study, a determination of (A, B) and its associated errors is dependent, to some extent, on the nature of the data used. The use of complex demodulation in conjunction with the Unit Vector Method (Everett & Hyndman 1967) allows all the records obtained at a particular station to be used in the fitting of (2). Such a process minimizes the undesirable effects of directional source bias and associated correlations between normal field components on the estimates of the transfer function (A, B). The approach to the determination of transfer function estimates outlined above is described by Banks (1975) and has been used throughout the present analysis. It should be noted that this method does not require a level of significance to be established; poor fits to (2) are reflected in the variance of the transfer function estimates as determined by the Unit Vector method.
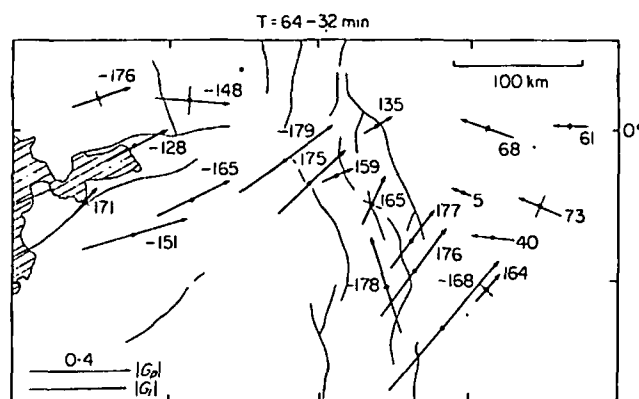
Figure 3. Vertical field single-station maximum and minimum response functions for the period band $T = 64-32$ min. Phases of the maximum axes are given in degrees.

3.2 SINGLE-STATION TRANSFER FUNCTIONS FOR THE KENYA ARRAY

Methods of presenting the information contained in transfer function estimates are discussed in more detail in Section 4. For the purpose of examining the effectiveness of single-station transfer functions, the maximum/minimum response function of Banks & Ottey (1974) are used. Maximum and minimum response functions, G_p and G_l respectively, were determined from the single-station transfer functions for the period bands described in Section 2. The results for the period band $T = 64-32$ min, are shown in Fig. 3. The arrows are perpendicular to the lateral boundary from which the anomalous vertical field derives, provided that the structure is two-dimensional. The lengths of the arrows indicate the magnitude of the anomalous vertical field associated with a unit amplitude disturbance, of zero phase, in the horizontal field. The phase of G_p along the eastern maximum axis (of E–W pointing arrows) is shown. For N–S arrows, the phase along the northern maximum axis is shown, thus delineating E–W structure. Two regions possessing very different response functions can be distinguished.

3.2.1 Western stations and the equatorial line

The response functions in the west and along the equatorial line of stations agree well with the results of Banks & Ottey (1974) and indicate an approximately N–S structure beneath the Rift graben. The western stations, with the exception of HBY (the western-most station), exhibit a similar azimuthal response and $|G_p|$ increases towards the Rift reaching a maximum on the western escarpment. Within the Rift floor, the vertical field is severely attenuated, indicating the presence of a region of enhanced conductivity beneath the Rift floor. To the east of the graben, the response $|G_p|$ again increases but is attenuated with respect to the western response. The E–W asymmetry of the response $|G_p|$ across the Rift axis is taken to indicate the presence of a region of enhanced conductivity to the east of the Rift graben. The phase of the maximum response at the western stations is consistent, being nearly 180° out of phase. Between the western flank (MOL) and the floor of the Rift (NAK), a phase change from negative out of phase to positive out of phase is observed. The phase then decays gradually to positive in-phase eastwards away from the Rift axis. The behaviour of the phase to the east of the Rift axis is suggestive of the mutual interaction of two conductive structures. This hypothesis is confirmed by the frequency response at TFL, on the eastern escarpment of the Rift. Fig. 4 shows both $|G_p|$ and $|G_l|$, the azimuth of G_p
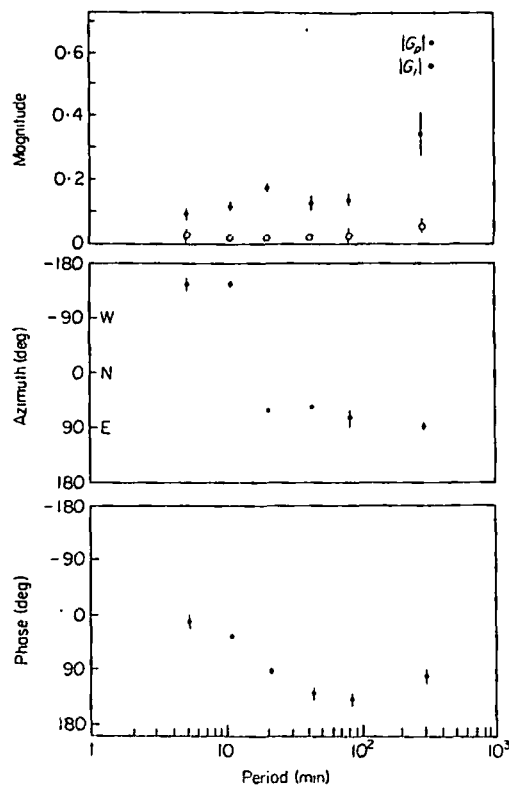
Figure 4. Magnitude, azimuth and phase of the vertical field single-station maximum response functions at Thompson's Falls (TFL) as a function of period. Magnitudes of the minimum response functions are shown as open circles. Error bars correspond to 1 sd.

and the phase of G_p, determined along the eastern maximum axis, at TFL for the period range $T = 512$–4 min. The error bars correspond to 1 sd about the mean. The magnitude of the response is relatively independent of frequency. The longest period estimate must be treated with caution since the period is comparable with the length of data and the estimates may be distorted by the removal of trends etc. At short periods (16–4 min) an in-phase response is observed and $|G_p|$ points towards the Rift axis, indicating the presence of a shallow conductor confined in lateral extent to the width of the present graben. At longer periods (> 20 min) the response at TFL is out of phase and G_p points eastward indicating the presence of a deeper eastern lateral boundary.

3.2.2 South-eastern stations

At the stations within the Rift, to the south of the equatorial line, and to the east of the Rift at NBI, the response shows a distinct change in character. The magnitude of the response increases progressively southwards, reaching a maximum at NBI where the anomalous vertical field is comparable in magnitude to the horizontal components of the field. The azimuth of the response along this line indicates a lateral boundary striking NW–SE from the zone of high conductivity beneath the Rift graben in the equatorial region. The south-eastern stations NYI, FHL and EMB possess response functions whose azimuths are similar to those of the eastern equatorial stations (NYK and MER) and indicate a roughly N–S boundary to the west. The phase of G_p at the two sets of stations is also similar indicating that the eastern conductor extends south at least as far as FHL.

It is clear that no simple two-dimensional boundary can be invoked to explain the observed response functions in the south-eastern region of the array. By its very nature, a two-dimensional boundary will produce response functions that are co-linear and perpendicular to the strike of the boundary (Lilley 1974). Thus it appears that both two- and three-dimensional conductivity structure exists within the array region. The non co-linear response functions are taken to indicate a three-dimensional structure and in such circumstances the presentation of transfer functions using induction vectors does not give a true picture of the internal current system.

3.3 THE PROBLEM OF ANOMALOUS HORIZONTAL FIELDS

Thus far we have ignored the possible bias introduced into the single-station transfer function (A, B) by the assumption $D_a \ll D$. As previously explained, this assumption is probably not valid for the data under consideration. In addition, the use of a single-station approach does not permit an assessment of the anomalous horizontal fields across the array. Both problems can be overcome using (1) if the normal field can be estimated. From the results presented so far it appears that certain of the western stations may be classified as normal; the criteria governing whether a station may be classified as normal are given by Banks (1973). Two reference normal stations were chosen using a coherence criterion (Beamish 1976). HBY and KSI, the western-most stations, exhibited the smallest anomalous horizontal fields of any array station. The use of two normal stations allows all the records used in the previous single-station analysis to be re-employed in the inter-station analysis. The normal field is assumed to be uniform across the array.

Equation (1) defines a matrix of transfer functions. An evaluation of all nine elements of T_{ij} is hindered by directionally polarized source fields leading to singularities of the matrix of cross-spectral terms required to calculate any one T (Dragert 1973). In addition, small elements within this matrix give rise to estimates of T_{ij} possessing a large error. Both of these problems arise in the case of Kenya data and it is still advantageous to assume that induction by Z_n can be ignored for each anomalous component.

3.4 VERTICAL FIELD INTER-STATION TRANSFER FUNCTIONS

Taking the third equation of (1) we have

$$Z_a = T_{ZH} H_n + T_{ZD} D_n + T_{ZZ} Z_n$$

at a particular frequency. The normal horizontal fields are taken to be those at one of the reference stations. We assume that Z_n is small and obtain the relationship

$$Z_c = T_{ZH} H_n + T_{ZD} D_n. \tag{3}$$

Thus we use exactly the same formulae to estimate (T_{ZH}, T_{ZD}) as for (A, B). It is worthwhile comparing the vertical field transfer functions obtained by single and inter-station methods. For simplicity we assume the constraint $Z_a \doteq Z$ to be exact. Comparison of the solution of (2) when the cross-spectra of the anomalous horizontal fields are included and the solution of (3) shows that if B is computed with large anomalous E—W fields present, the effect will be to decrease the magnitude of B observed. When normal horizontal fields are used in the calculation we expect the transfer function (T_{ZH}, T_{ZD}) to have a larger magnitude with an azimuth tending towards a more E—W orientation when compared to (A, B). If the predominant anomalous fields are observed in the N—S field, again a larger transfer function (T_{ZH}, T_{ZD}) would result but with an azimuth tending to a more N—S orientation.
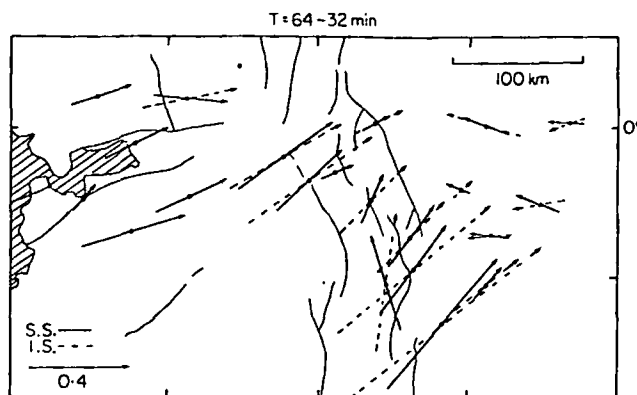
Figure 5. Comparison of the vertical field maximum response functions obtained by single-station and inter-station methods. Period band $T = 64-32$ min.

Inter-station vertical field transfer functions were computed across the array using the horizontal fields recorded at either HBY or KSI. The computational procedure was identical to that used for the single-station analysis. It should be noted that when inter-station methods are used a greater degree of care must be taken to ensure accurate timing otherwise a phase-shift varying linearly with frequency is introduced into the cross-spectra. Maximum and minimum response functions are again used to present the transfer function estimates. Fig. 5 is a comparison of the maximum vertical field response functions ($|G_p|$) obtained by single-station (SS) and inter-station (IS) methods, for the period band $T = 64-32$ min. A large number of quantitative differences exist that are significant, i.e. greater than the variance in the response functions as determined by the Unit Vector method. The two response functions at BUT (the most westerly station at which a comparison is made) are identical, confirming the lack of anomalous horizontal fields in this region. Over the rest of the array, with the exception of LGT, the increased magnitude and swing of azimuth of the inter-station response functions indicate that the anomalous horizontal fields are due to predominantly N–S striking currents. LGT has a single-station response that indicates local E–W anomalous currents are responsible. The reversal at NYI is not significant, the phase being such that the direction is indeterminate. The largest anomalous horizontal fields appear in the south of the array, in the NBI region.

3.5 HORIZONTAL FIELD INTER-STATION TRANSFER FUNCTIONS

Since the predominant anomalous horizontal fields are observed in the E–W component, only anomalous D field transfer functions were estimated. The second equation of (1) characterizing the anomalous D component of the field is

$$D_a = T_{DH} H_n + T_{DD} D_n + T_{DZ} Z_n$$

at a particular frequency. On specifying the constraint that Z_n is small, we obtain

$$D_a = T_{DH} H_n + T_{DD} D_n + \epsilon \tag{4}$$

where ϵ represents the residual part of D_a that does not correlate with either H_n or D_n. Since we wish to use the total recorded field, $D = D_a + D_n$, observed at each station a further substitution is required. If we assume $D_a \doteq D$, i.e. D_n is small, on taking cross-spectra of D

with $H_n{}^*$ and $D_n{}^*$ in turn (* denotes complex conjugate) and minimizing the residual error term, we obtain

$$T_{DH} = (S_{DH_n}S_{D_nD_n} - S_{DD_n}S_{D_nH_n})/(S_{D_nD_n}S_{H_nH_n} - S_{D_nH_n}S_{H_nD_n})$$

$$T_{DD} = (S_{DD_n}S_{H_nH_n} - S_{DH_n}S_{H_nD_n})/(S_{D_nD_n}S_{H_nH_n} - S_{D_nH_n}S_{H_nD_n}) \tag{5}$$

where S_{DH_n} denotes the cross-spectrum of $D(t)$ and $H_n(t)$ at a particular frequency. Alternatively, if the substitution $D_a = D - D_n$ is made in (4), the expression for T_{DH} remains as in (5) and the expression for T_{DD} becomes

$$T'_{DD} = [(S_{DD_n}S_{H_nH_n} - S_{DH_n}S_{H_nD_n})/(S_{D_nD_n}S_{H_nH_n} - S_{DH_n}S_{H_nD_n})] - 1.$$

Hence $T'_{DD} = T_{DD} - 1$ and the second method gives a transfer function (T_{DH}, T'_{DD}) that does not include the normal component of the D variation field recorded at each station. The transfer function in the normal region, in this case is zero. (T_{DH}, T_{DD}) however does include D_n and values of $(T_{DH}, T_{DD}) > 1$ are produced when the D component possesses an anomalous contribution. A normal station would possess a transfer function (T_{DH}, T_{DD}) of $T_{DH} = 0, T_{DD} = 1$.

Inter-station horizontal field transfer functions defined by (5) were computed across the array using the horizontal fields recorded at either HBY or KSI. The same sets of data were used as for the determination of the vertical field inter-station transfer functions and the computational procedure was identical. Maximum and minimum response functions can be deduced from the horizontal field inter-station transfer functions (T_{DH}, T_{DD}). This might provide a method of presentation whereby the anomalous internal current contribution to the D component can be assessed. However due to the fact that the D variation field is naturally constrained to a particular horizontal direction, no information is gained concerning the local orientation of conductive boundaries as is obtained from vertical field transfer functions. To obtain such information both H_a and D_a must be known. When only one anomalous horizontal field component is available an alternative method of presentation is required.

4 Presentation of transfer functions

In the previous section we have discussed the factors influencing accurate and unbiased estimates of both single-station and inter-station transfer functions. Using such estimates we have adopted an induction vector representation, namely maximum and minimum response functions, in order to elucidate the lateral variation in conductivity in East Africa. The results indicate that both two- and three-dimensional conductivity contrasts are present. In such circumstances, the significance of the induction vectors is not always obvious. In the case of three-dimensional structure it is found that an alternative method termed Hypothetical Event Analysis is the most useful and informative method of presentation.

4.1 INDUCTION VECTOR PRESENTATION

The fitting of an equation of the type $Z_c = AH + BD$ to the observed field data defines a preferred plane along which magnetic field variations, at a particular frequency, tend to occur (Parkinson 1959). From the amplitude and phase information incorporated in the plane (A, B), induction vectors can be formed which when plotted in the horizontal plane point towards internal concentrations of current. Two different types of induction vector

he residual error

(5)

cular frequency.
for T_{DH} remains

T_{DH}, T'_{DD}) that
at each station.
$_D$) however does
nent possesses an
n (T_{DH}, T_{DD}) of

computed across
ame sets of data
er functions and
ise functions can
r_{DD}). This might
contribution to
variation field is
s gained concern-
ical field transfer
When only one
if presentation is

ite and unbiased
g such estimates
n and minimum
ty in East Africa.
rasts are present.
ways obvious. In
od termed Hypo-
tation.

ld data defines a
quency, tend to
orporated in the
horizontal plane
induction vector

representation exist which are aimed at separating anomalous fields of different origins. The separation of (A, B) into in-phase and quadrature parts to form real and imaginary induction vectors is essentially aimed at separating the effects of deep and shallow anomalies (Schmucker 1970; Gough 1973). For bodies of widely differing dimensions it should be possible to observe both the inductive limit (in-phase response) and the resistive limit (quadrature response) using this method. The maximum and minimum response functions of Banks & Ottey (1974) are aimed at separating from (A, B) that part of the response that is compatible with a two-dimensional assumption. This information is directly incorporated into the maximum response function G_p. G_p is then interpretable in terms of the perturbation of regional horizontal current flow by a two-dimensional conductive boundary as formulated by Jones & Price (1970). Both induction vector presentations have a simple interpretation only when the structure is two-dimensional (see Banks 1973). In such circumstances the vectors point towards the conductive boundaries that define the E-polarization mode of Jones & Price (1970). With reference to Fig. 3 in which the maximum and minimum response functions $(G_p$ and $G_l)$ for the period band $T = 64-32$ min are shown, the approximate co-linearity of G_p across the equatorial profile together with the fact that $G_p \succ G_l$ suggests that the response functions are meaningful in this region. In the south-eastern region however the azimuths of G_p show a large variation over distances of the order of 50 km and it is clearly not obvious where the conductive boundaries are situated. When non-parallel maximum response functions are present they can only be taken to indicate a three-dimensional situation and a method of displaying the anomalous fields themselves is required thus allowing an interpretation in terms of three-dimensional current flow.

4.2 HYPOTHETICAL EVENT ANALYSIS (HEA)

This method of presentation was suggested by Bailey *et al.* (1975) and applied to vertical field single-station transfer functions obtained from non-simultaneous station operation in Eastern Canada. The method has since been successfully applied to similar transfer function estimates across the UK (Bailey & Edwards 1976). Hypothetical event analysis is the calculation of the anomalous fields that would be associated with a unit amplitude event of a given polarization in the horizontal field. Bailey *et al.* point out that a naive method of calculating Z_c for a hypothetical horizontal field is to postulate the same horizontal field at each station and calculate Z_c from (2). They discuss the objections to this and conclude that the naive method is justified if the horizontal field is essentially uniform over the region under consideration. There is, however, a possible extension to this method that allows for non-uniform horizontal fields across the array region when simultaneous recording is available. A reference station can be used such that all transfer functions are calculated with respect to the horizontal fields recorded at the reference station. Ideally a reference station that is normal would be chosen, although this is not strictly required. The use of a reference station that is normal simplifies subsequent interpretation since then the transfer functions would be the set of T's of equation (1).

In theory at least, all three anomalous field components H_a, D_a and Z_a can be determined directly using transfer functions computed with respect to the horizontal fields recorded at the reference station. In the previous section a set of transfer functions characterizing Z_a and D_a have been determined using the horizontal fields recorded at the two normal stations, HBY and KSI. Using the hypothetical event method of presentation, the transfer functions (T_{ZH}, T_{ZD}) and (T_{DH}, T_{DD}) can be used to map the dependence of the anomalous Z and D component fields on the azimuth of linearly polarized regional horizontal fields. Consider first the anomalous vertical field (Z_c) given by (3). A unit horizontal field disturbance

at an angle θ to magnetic north is resolved into (H_n, D_n). Since Z_c is complex, the hypothetical response may be separated into real and imaginary parts

$$Z_R(\theta) = \text{Re}\,[T_{ZH}]\cos\theta + \text{Re}\,[T_{ZD}]\sin\theta$$

$$Z_I(\theta) = \text{Im}\,[T_{ZH}]\cos\theta + \text{Im}\,[T_{ZD}]\sin\theta.$$

$$\tag{6}$$

Alternatively the modulus and phase of the vertical field response may be determined

$$|Z(\theta)|^2 = [Z_R(\theta)]^2 + [Z_I(\theta)]^2$$

$$\phi(\theta) = \tan^{-1}\,[Z_I(\theta)/Z_R(\theta)].$$

$$\tag{7}$$

The fields we map are the vertical and E–W components of the field produced by the anomalous internal current flow when the regional field is linearly polarized at azimuth θ, i.e. when the regional current flow far from the array is uniform and has an azimuth $\theta + 90°$. This uniform regional current flow is perturbed by lateral variations in conductivity structure giving rise to local anomalous and horizontal field variations. The method of presentation makes no assumptions concerning the geometry of the conductive structure under consideration and hence the method possesses the ability to cope with both two- and three-dimensional conductivity structures. For approximately two-dimensional conductivity contrasts, a maximum response will be observed for the E-polarization mode, i.e. when the hypothetical event is polarized perpendicular to the conductive boundary. For a polarization orthogonal to this, no effect due to the boundary should be observable. A response due to departures from two-dimensionality in which lateral variations consistently deflect or channel current should be observable for all polarizations of the hypothetical event.

The interpretation of this method of presentation requires a form of response map inversion, i.e. we seek the internal current system from which the anomalous field components derive. This inverse problem may be approached qualitatively by reference to the equivalent internal current system analogous to that used in the study of the morphology of external current systems (see, e.g. Matsushita 1967). The equivalent internal current system consists of an electric field poloidal mode directly analogous to the E-polarization mode of Jones & Price (1970). In such a partial system no vertical current flow exists and the internal field parameters presented by hypothetical event analysis may therefore be interpreted in terms of an equivalent internal current system which flows parallel to the surface of the Earth in a thin layer. Such thin-sheet descriptions are characterized by horizontal currents forming closed loops (Price 1949). If the horizontal divergence of the current is non-zero and vertical current flow exists the current vortices associated with the thin sheet problem would no longer be evidenced.

4.3 VERTICAL COMPONENT RESPONSE MAPS

The vertical field response defined by (6) and (7) was determined across the array. This produced four response maps for each azimuth of the hypothetical event. The response to a linearly polarized field can be determined as the resultant of two orthogonal polarizations and we here consider a range of hypothetical events polarized in the range 0–90° (azimuths are measured positive eastwards from magnetic north). Useful results can only be obtained when the station spacing is less than or of the same order as the spatial structure of the equivalent internal current system. Regions of uncertainty will be indicated by broken contours.
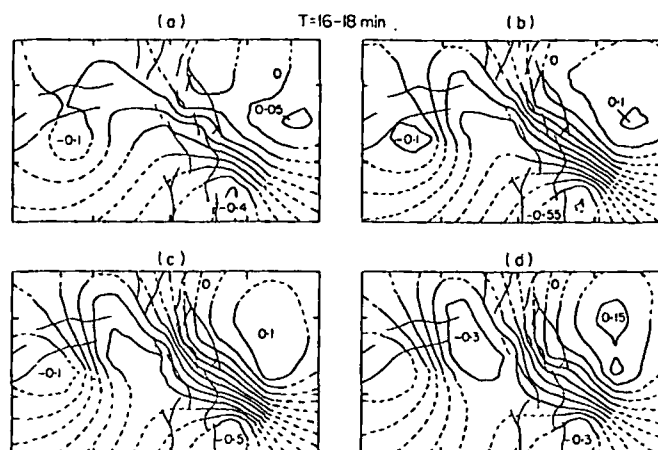
Figure 6. Real part of the vertical field response to four linear horizontal field polarizations; (a) $\theta = 0°$; (b) $\theta = 30°$; (c) $\theta = 60°$; (d) $\theta = 90°$. Period band $T = 16-8$ min. Contour interval is 0.05 nT.

Fig. 6 shows the real part of the vertical field Z_R in the period band $T = 16-8$ min, associated with four polarizations of the horizontal field in the range $\theta = 0-90°$. A prominent feature of all four polarizations is the steep field gradients observed in the south-east region. The causative current system must therefore be independent of the direction of the regional normal field, indicating that the conductive boundary is capable of deflecting the regional current flow. The current system in this region has both N-S and E-W components and the conductive boundary appears to concentrate the current flow in the NBI/TKA region, giving rise to the large spatial gradient in Z_R. The spatial gradient of Z_R is a maximum for $\theta = 30-60°$; a corresponding minimum was found for polarizations of $\theta = -30$ to $-60°$. Thus the general strike of the conductor in the south-eastern region is NW-SE. The map for a polarization of $\theta = 90°$ (regional current flow N-S) indicates a N-S striking boundary coincident with the Rift axis in the equatorial region. $Z_R(\theta)$ is polarization dependent in this region, being diffuse for $\theta = 0°$ and increasing in definition with the increase of θ. The total current system produced by this conductor varies with the azimuth of the regional field and hence the observed response is compatible with the varying fractions of the E-polarization mode which would be produced by a N-S striking two-dimensional boundary.

The conductivity structure in both regions is well-defined by the polarization of $\theta = 90°$. The transition from negative values of Z_R in the west to positive values in the east is taken to indicate the edge of a conductive boundary. Both Z_R and Z_I (not shown) delineate the same conductivity structure and it was found that the most appropriate response parameters were $|Z(\theta)|$ and $\phi(\theta)$. Having noted the azimuthal dependence of the anomalous vertical field, we confine our attention to a polarization of $\theta = 90°$ which adequately describes the internal current system across the array.

Fig. 7 shows $|Z(\theta)|$ for the period band $T = 64-32$ min, for a hypothetical event of $\theta = 90°$. A line current will produce an anomalous vertical field with contours running parallel to the strike of the current. In the equatorial region, the central contours are coincident with the Rift graben and an E-W asymmetry about the Rift axis is evident. The region of the west of the Rift is regarded as normal; the lack of symmetry due to the equivalent edge-effect current is then evident to the east of the Rift graben in the equatorial region and to the north-east of the NBI region. The magnitude of the anomalous vertical field is attenuated across this region. The contours are smooth and of a large scale and can
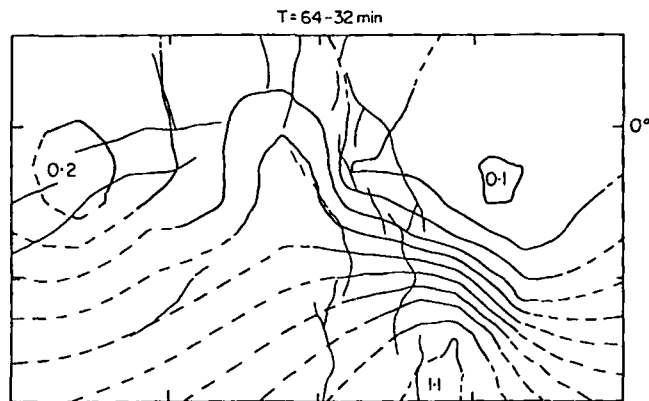
Figure 7. Modulus of the vertical field response to a linear horizontal field polarization of $\theta = 90°$. Period band $T = 64-32$ min. Contour interval is 0.1 nT.
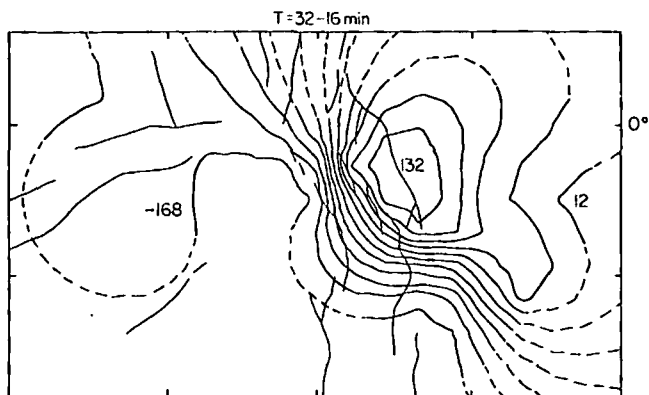

Figure 8. Phase of the vertical field response to a linear horizontal field polarization of $\theta = 90°$. Period band $T = 32-16$ min. Contour interval is 30°.

therefore be attributed to an extended sheet of enhanced conductivity containing a diffuse current system. To the south of the equatorial Rift axis, internal current flow is directed NW—SE away from the central graben, producing a large vertical field gradient in the NBI region. The spatial gradients in the vertical field of the equivalent internal current system *flowing in a thin surface sheet are proportional to the local current density.* The large gradients in the south-east are therefore to be associated with an exceptionally high conductivity contrast and/or an intense local geometrical concentration of current. The azimuthal response to hypothetical events indicates at least part of the effect must be produced by the latter.

The phase of the response $\phi(\theta)$ to a hypothetical event ($\theta = 90°$) for the period band $T = 32-16$ min is shown in Fig. 8. The western normal region possesses a negative and out-of-phase response that shows only slight lateral modification. In the immediate vicinity of the western flank of the Rift, in the equatorial region, there is a sharp phase reversal to in-phase within the Rift floor. A transition to positive out-of-phase response then occurs at the eastern escarpment. Eastwards, away from the Rift axis, the phase gradually decays to an in-phase response. In terms of the equivalent internal current system, a phase change of π in the anomalous vertical field should be observed across a current concentration. The complex behaviour of $\phi(\theta)$ across the equatorial profile is taken to indicate the mutual interaction between currents beneath the Rift floor and an extended current system to the

east. In the south-east a phase change of π is observed across a SW—NE profile indicating that there is a single current concentration in this region.

4.4 HORIZONTAL COMPONENT RESPONSE MAPS

The horizontal D component response to hypothetical events is calculated by replacing T_{ZH} and T_{ZD} in (6) by T_{DH} and T_{DD}, respectively. The preceding interpretation has indicated that anomalous current flow is directed predominantly N—S in the equatorial region. In the south-east both N—S and E—W components of current flow exist. It should therefore be possible to utilize the polarization dependence of the anomalous D component field to resolve these two features separately. From the way in which the D component inter-station transfer functions are defined, a hypothetical event polarized N—S ($\theta = 0°$) will correspond to a D component response at a normal station of zero amplitude and phase. A hypothetical event with $\theta = 90°$ will produce a D component response of amplitude unity and zero phase at a normal station. It should be emphasized that anomalous fields in the D component can only be produced by internal currents possessing a N—S component of current flow.

Fig. 9 shows the modulus of the D component response in the period range $T = 32$—16 min, to four polarizations of the regional horizontal field E—W regional current flow ($\theta = 0°$) is seen to produce an anomaly confined to the eastern portion of the array. In order to produce this anomaly in the D component, normal E—W current flow must be deflected such that a N—S component of current flow is produced. When compared to other polarizations, the anomaly in the south-eastern region for $\theta = 0°$ is seen to be diffuse indicating that the major portion of current flow is still directed E—W. This conclusion is compatible with regional current flow entering the array region and being channelled into a NW—SE orientation in the area of NBI/TKA. As the polarization angle increases to $\theta = 90°$ and regional current flow is directed into a N—S orientation, the anomaly in the south-east is seen to increase in definition in accord with the major portion of current flow being directed NW—SE. A prominent feature of these maps is the dependence of the equatorial response on azimuth. For E—W regional current flow ($\theta = 0°$) it is entirely absent while for N—S regional current flow it is well-defined, indicating that the response is due to N—S currents flowing along a two-dimensional boundary. The centre of enhanced D lies to the
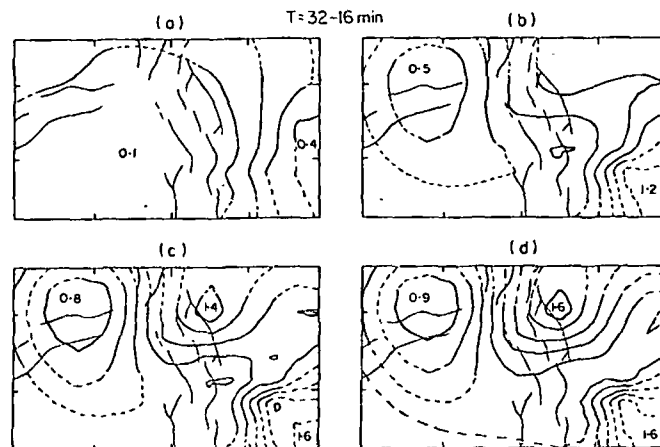

Figure 9. Modulus of the D component response to four linear horizontal field polarizations; (a) $\theta = 0°$; (b) $\theta = 30°$; (c) $\theta = 60°$; (d) $\theta = 90°$. Period band $T = 32$—16 min. Contour interval is $0.1\,nT$.
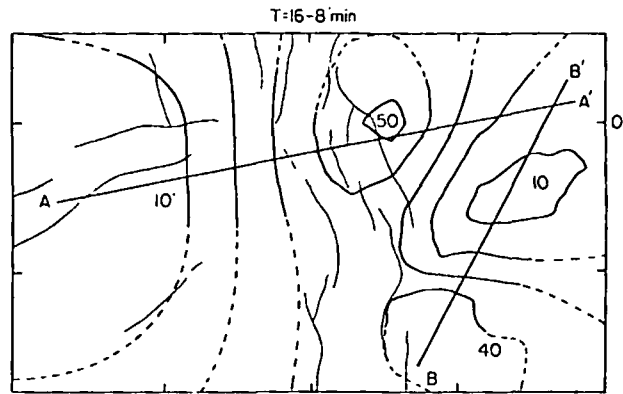
Figure 10. Phase of the *D* component response to a linear horizontal field polarization of $\theta = 90°$. Period band $T = 16-8$ min. Contour interval is $10°$.

east of the Rift graben. The response to the west, compatible with a N—S striking boundary, falls off to a value of unity in the normal region. The response to the east of the central maximum reveals an E—W asymmetry. Such an asymmetry again indicates the mutual interaction between a current system within a body beneath the Rift floor and an extensive current system to the east. The contours of the equatorial maximum close and run E—W in the region of NVA indicating that N—S current flow terminates in this region even when the regional current flow is directed N—S. The internal currents must therefore be deflected locally E—W in the NVA region and hence must couple with the E—W current flow observed to the north of the NBI/TKA region. As in the case of the vertical field analysis, this argues for a body associated with the Rift graben that extends south only as far as the NVA region.

Fig. 10 shows the phase of the anomalous *D* component field for a hypothetical event polarization of $\theta = 90°$ in the period band $T = 16-8$ min. This polarization introduces N—S regional current flow into the array area; the normal nature of the region to the west of the Rift graben is clearly evidenced. The maximum anomalous phase occurs to the east of the Rift graben and can be accounted for by the mutual interaction and reinforcement of currents within the Rift axial body and a current system to the east. In the south-eastern region the lack of N—S current flow is evident. The N—S regional current flow is deflected into a predominantly E—W orientation in the region of NBI/TKA. The closed contour of $10°$ to the north-east of NBI can be accounted for by the predominance of the south-eastern anomaly rather than the extended current system. It is clear that any deeper structure in the south-eastern region will inevitably be masked by the larger current concentration effects, assumed to be crustal.

4.5 COMPARISON OF HEA AND FOURIER RESPONSE MAP PRESENTATIONS

HEA based on inter-station transfer functions is capable of obtaining anomalous response maps in three field components and could be construed as being a similar method of presentation to maps of Fourier spectral components (see Gough 1973), thus far not discussed. This method requires simultaneous recording at each station across the array. Individual events, such as bay activity, are selected from the recorded data and Fourier transformed directly. The method produces six contour maps: three Fourier amplitude and three Fourier phase maps in either geomagnetic or geographic coordinates. Since it is the internal response that is required, it is considered that if the spatial scale of anomalies are consistent for independent source fields (at the same period) then they can be ascribed to

o°

ation of $\theta = 90°$. Period

S striking boundary,
e east of the central
ndicates the mutual
oor and an extensive
lose and run E—W in
is region even when
erefore be deflected
irrent flow observed
analysis, this argues
as the NVA region.
hypothetical event
ion introduces N—S
n to the west of the
s to the east of the
d reinforcement of
n the south-eastern
nt flow is deflected
ised contour of 10°
f the south-eastern
per structure in the
ncentration effects,

TATIONS

nomalous response
similar method of
73), thus far not
across the array.
data and Fourier
rier amplitude and
les. Since it is the
: of anomalies are
:an be ascribed to

internal structure (Gough 1973). If the spatial configuration of each magnetic field disturbance can be considered stationary, a polarization of the horizontal field can be defined (Lilley & Bennett 1972). Individual events can then be used to examine the dependence of the Fourier response maps on the polarization of the horizontal field. Such a study has been carried out in Southern Australia (Gough, Lilley & McElhinny 1972; Gough, McElhinny & Lilley 1974). The horizontal field polarization of recorded events is complex with three parameters to be specified: azimuth, ellipticity and sense of rotation. Gough *et al.* (1974) found a complicated dependence of Fourier map structure on all three parameters. Although the exact relationship between anomalous structure and the polarization parameters was not clear, a three-dimensional conductivity structure was indicated. With regard to the ability of Fourier response maps and hypothetical event maps to define magnetic variation anomalies we note the following characteristics. Problems inherent in the Fourier response map method include:

(1) The anomalous contribution to the variation fields may not be effectively separated.

(2) A large number of individual events is required to define the response to an adequate range of horizontal field polarizations.

(3) In general, three parameters need to be specified to define the polarization of the recorded horizontal fields. The response maps for circularly and elliptically polarized events are not so easy to analyse as those for linearly polarized events.

HEA based on inter-station transfer functions has the ability to overcome these difficulties in that:

(1) Transfer function analysis can effectively separate the anomalous parts of the variation fields.

(2) The internal response is defined for all horizontal field polarizations.

(3) The use of hypothetical events enables the internal response to be mapped for linear polarizations of the horizontal field.

5 Depths of currents

Estimates of the maximum depths of internal currents can be made by assuming the anomalous fields to be produced by an equivalent line current at depth d. Such a line current would produce an anomalous field of width $2d$ at the half-maximum value and an anomalous vertical field with extrema $2d$ apart. The actual line current cannot be deeper than the equivalent line current best-fitting the anomaly widths (Gough 1973). In the case of extended conductors, the anomalous vertical field delineates the edges of the body while the anomalous horizontal field can be used as a measure of its lateral extent.

5.1 EQUATORIAL PROFILE

Having established that a two-dimensional assumption is justified across an E—W equatorial profile, the dependence of the anomalous fields on period is now considered. A profile $A-A'$, shown in Fig. 10 was chosen orthogonal to the conductive boundary as deduced in the preceding sections. The inter-station maximum response functions about this profile then define $|Z_a/H_n|$ and $|D_a/H_n|$ where H_n is a unit normal horizontal field disturbance. Stations whose estimates were based on only one record were not included. HBY is not included in the vertical field estimates because the direction of maximum correlation is not along the profile.
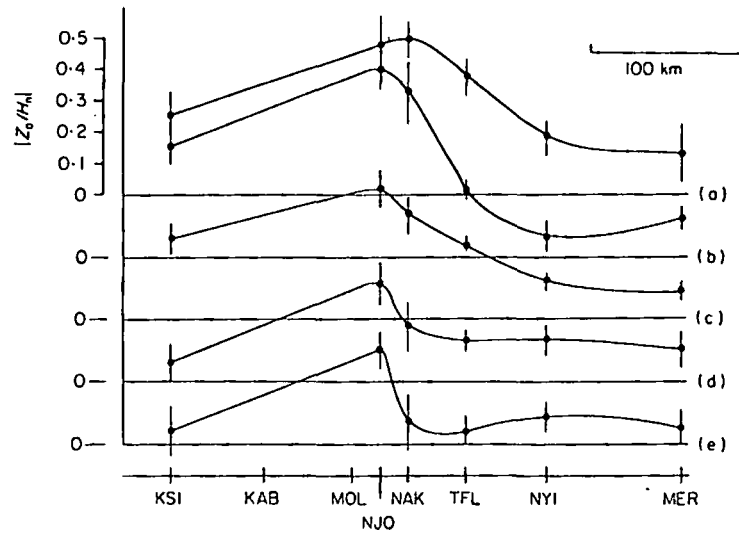
Figure 11. Vertical field inter-station maximum response functions along the profile $A-A'$ in the period bands; (a) 128–64; (b) 64–32; (c) 32–16; (d) 16–8; (e) 8–4 min. Error bars correspond to 1 sd.

Fig. 11 shows $|Z_a/H_n|$ determined along the profile for the period bands in the range $T = 128$–4 min. Error bars correspond to 1 sd about the mean. For all periods a maximum response occurs on the western flank of the Rift at NJO, and the asymmetry of the anomaly indicates that a conductive boundary must extend eastwards beyond the eastern escarpment of the Rift. The relatively small lateral scale of the anomaly over the Rift region in the period band $T = 16$–4 min indicates a concentration of current flowing beneath the Rift floor. The equivalent line current at depth d would produce Z extreme $2d$ apart; however no one wavelength is fully defined due to the asymmetry. The shorter wavelength feature is however best defined in the period band $T = 8$–4 min and it seems likely that the Z extreme can be no more than 60 km apart and hence the actual current cannot be deeper than ~ 30 km. This estimate suggests a conductive body within the crust directly beneath the Rift floor. The attenuation in the anomalous vertical field observed in the east for all periods is consistent with an extensive body of large dimensions beneath the region to the east of the Rift graben.

Fig. 12 shows $|D_a/H_n|$ along the profile $A-A'$ for the same period bands. Error bars again correspond to 1 sd. There is a relatively uniform increase of response with period; the maximum response being observed at TFL for all periods. The fact that the maximum is observed to the east of the Rift axis indicates that the response is the resultant of the mutual interaction of currents within a Rift axial conductor and an eastward extending current system. With this factor in mind, it is possible to estimate the depth d of the equivalent line-current producing a variation in the D component of width $2d$ at the half-maximum. For the period range $T = 128$–16 min, d is of the order of 50 km. If two bodies at different depths are responsible, the depth d represents an intermediate depth, placing the eastern conductor well within the upper mantle.

5.2 THE SOUTH-EAST REGION

It is informative to compare the vertical field response observed in the equatorial region with that observed in the south-eastern region. With only single-station transfer function estimates it would be difficult to establish a profile in the south-eastern region, however we
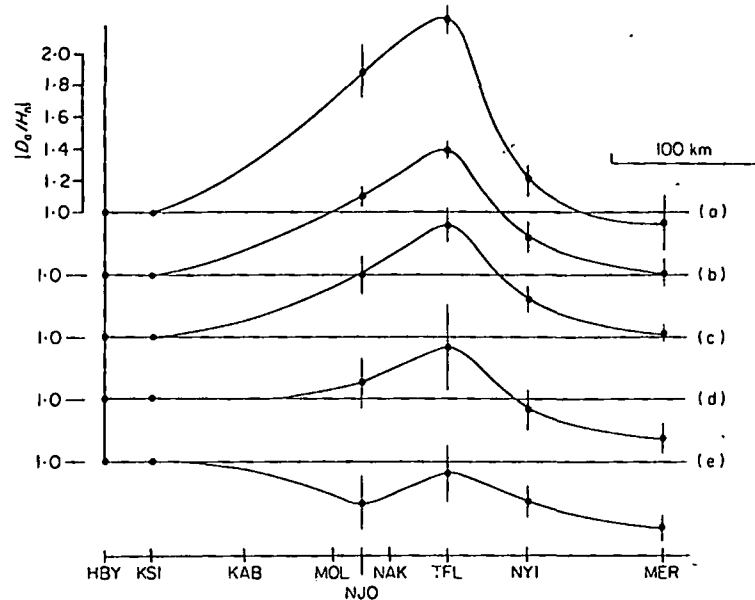
Figure 12. D component inter-station maximum response functions along the profile $A-A'$ in the period bands; (a) 128–64; (b) 64–32; (c) 32–16; (d) 16–8; (e) 8–4 min. Error bars correspond to 1 sd.

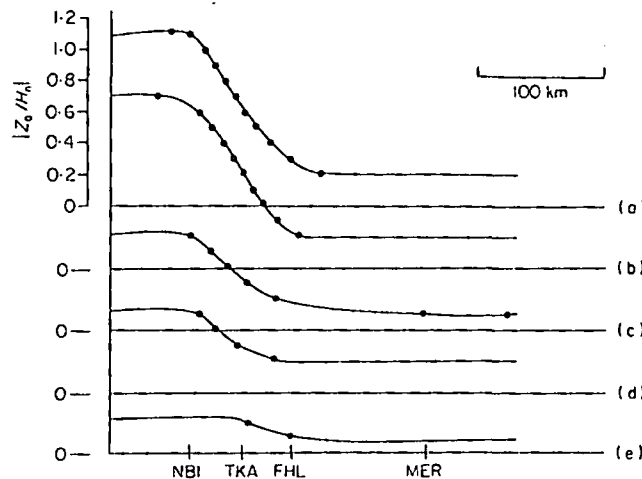
Figure 13. Interpolated vertical field response to a linear horizontal field polarization of $\theta = 60°$, along the profile $B-B'$. Period bands are; (a) 128–64; (b) 64–32; (c) 32–16; (d) 16–8; (e) 8–4 min.

can make use of the hypothetical event maps to determine a profile. Although such a profile is subject to an interpolation procedure and is necessarily a smoothed version of the actual response estimates, it is useful in establishing the general features of the response with period. A profile $B-B'$ was chosen perpendicular to the NW–SE axis of symmetry shown in Fig. 10. Fig. 13 then represents the smoothed behaviour of $|Z_a/H_n|$ along the profile $B-B'$ in the period range $T = 128–4$ min. The edge of the conductor appears slightly to the south of TKA and the anomalous vertical field reaches a minimum in the region of FHL. In the region to the north-east of FHL there appears to be little or no variation in the observed response indicating that the region is underlain by a major conductor. There is a large

increase in the vertical field between the period bands $T = 32-16$ min and $T = 64-32$ min. The response in this region is associated with a conductive boundary constraining the currents to flow NW−SE in the NBI/TKA area. This boundary possesses a larger vertical field response for each period band than that observed in the equatorial zone. It is reasonable to assume that a geometrical concentration of current causes the large spatial gradients in the vertical field. The wavelength of the anomaly is not fully defined but, as outlined below, the response is consistent with a crustal source.

5.3 FREQUENCY DEPENDENCE OF THE ANOMALOUS FIELDS

Figs 11 and 12 show that the magnitude of the vertical and horizontal anomalous fields across the equatorial profile increases with period in the range $T = 128-4$ min. A much larger increase in the magnitude of Z_a with period is observed in the south-eastern region (Fig. 13). It is difficult to envisage any induction process embodying a skin−depth relationship which can account for the observed anomalous fields over the entire period range of the analysis. The observed response with period can be explained however if the anomalous internal current system at the longer periods is the result of the resistive channelling of regionally induced currents. This hypothesis was originally put forward by Dyck & Garland (1969) to explain certain features of the Alert anomaly. The currents are assumed to result from large-scale induction over an area much larger than the region under consideration. If the skin−depth is large compared to the dimensions of a structure (i.e. self-induction can be ignored) then curl $\mathbf{E} \doteq 0$ and we can write $\mathbf{E} = -\nabla\phi$. The distribution of internal currents can thus be obtained by solving the Laplace equation rather than the vector diffusion equation. In comparison to the case formulated by Jones & Price (1970) in which a body is immersed in an alternating electric field and which gives rise to a frequency-dependent response, current channelling as invoked by Dyck & Garland (1969) implies the body is immersed in a uniform dc electric field and the response should be independent to frequency. To differentiate the two cases, it would seem appropriate to call the dc effect, caused by source fields possessing skin−depths far greater than the dimensions of the body, resistive current-channelling.

Depending on the geometry of anomalous regions, it is possible for the channelled currents to become concentrated thereby producing much larger anomalous fields than can be accounted for by normal induction mechanisms (Gough 1973). Crustal structures are generally to be associated with smaller scale lengths than deeper upper mantle inhomogeneities and hence crustal structure should be more susceptible to the frequency-independent limit of resistive current channelling. It is proposed that at periods of 4−32 min, the self-inductance of the sub-Rift conductor is not negligible. At longer periods however, the response is determined by resistive current-channelling as outlined above. The additional current concentration at long periods then explains the increase in the magnitude of the anomalous fields noted in Figs 11 and 12. The exceptional increase with period in the magnitude of Z_a in the south-eastern region is similarly consistent with the geometrical concentration of resistivity channelled current-flow in a three-dimensional conductivity structure.

6 Conclusions

Both single-station and inter-station transfer function estimates have been utilized to investigate lateral conductivity structure in East Africa. The derivation of transfer function estimates using the technique of complex demodulation together with the Unit Vector

| T = 64–32 min.
constraining the
rger vertical field
t is reasonable to
gradients in the
tlined below, the

anomalous fields
4 min. A much
th-eastern region
– depth relation-
riod range of the
' the anomalous
; channelling of
Dyck & Garland
ssumed to result
r consideration.
If-induction can
nternal currents
ector diffusion
which a body is
y-dependent re-
ics the body is
independent to
I the dc effect,
ns of the body.,

the channelled
fields than can
structures are
antle inhomo-
the frequency-
ls of 4–32 min,
riods however,
The additional
gnitude of the
period in the
ie geometrical
I conductivity

utilized to in-
ssfer function
: Unit Vector

method of calculating transfer functions has proven to be advantageous for the data under consideration in which source field bias is severe. In East Africa it is found that anomalous horizontal fields are comparable with the normal variation field. In such circumstances single-station transfer function estimates are not strictly valid and it is necessary to determine inter-station transfer function estimates. Two methods of presenting the information contained in the transfer function estimates have been employed. Both methods are capable of defining anomalous internal variation fields in three components if inter-station transfer functions are available. The first method involves an induction vector representation. The amplitude and phase information presented by this method is meaningful only in the case of two-dimensional structure. The second method of presentation is termed hypothetical event analysis. This method maps the dependence of the anomalous field components to linear polarizations of the regional horizontal field and is therefore capable of establishing whether or not a particular boundary can be considered two-dimensional. Both vertical and horizontal anomalous fields can be directly mapped across the array region with no assumptions concerning the geometry of the conductive configuration under consideration. Both two- and three-dimensional conductivity contrasts are encountered in East Africa and the second method has proven to be the only viable method for the determination of the lateral conductive boundaries across the array region. Considerable constraints on the uniqueness of the conductivity distribution have been achieved by an examination of the anomalous horizontal field response maps presented by this method. In the case of the Rift axial body, additional information has been gained with regard to its lateral extent. The response maps may be interpreted in terms of an equivalent internal current system analogous to that used in the study of the morphology of exter..al current systems. Although treated only qualitatively in the present paper, the response maps of hypothetical event analysis could form the basis for a quantitative approach to the inverse problem.

The inferred pattern of current flow seems to require three distinct regions of enhanced conductivity within and to the east of the Gregory Rift. These results are summarized in Fig. 14, the regions of uncertainty being indicated. Across an E–W equatorial profile $(A–A')$, the conductivity distribution is approximately two-dimensional, the major boundaries striking N–S. Across this profile two distinct conductive bodies are evident:

(1) A crustal Rift axial body limited in lateral extent to roughly the size of the present Rift boundary faults. This body appears to be relatively localized, coincident with the Rift axis only as far as $0° 50' S$.
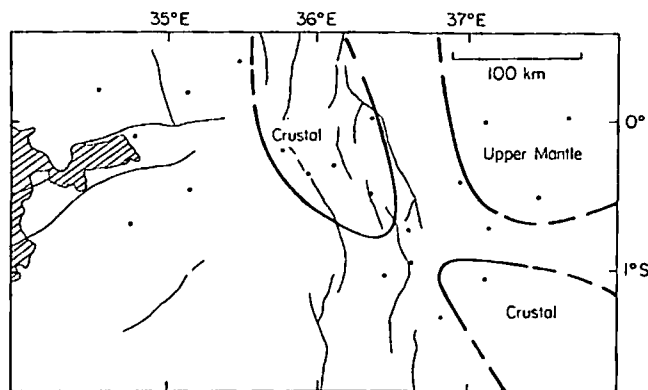

Figure 14. The lateral variation in conductivity structure across East Africa. Regions of anomalously high conductivity are outlined. Broken contours indicate regions of uncertainty.

(2) An extensive region of enhanced conductivity exists to the east of the Rift graben. This region lies within the upper mantle. The eastward extent of this region is undefined by the present array experiment.

A third conductive body lies in the south-eastern region of the array:

(3) To the east of Nairobi, a NW–SE zone of high conductivity exists which possesses a three-dimensional boundary. Regionally induced currents appear to be channelled into the two equatorial bodies by this conductor. The lateral extent of this body along its strike is undefined. The internal field characteristics of this body suggest it is to be associated with exceptional crustal conditions. The depth profiles of these anomalous regions, their conductivities together with their implications regarding the physical state of the crust and upper mantle across East Africa will be discussed in a later paper.

Acknowledgments

References

Bailey, R. C., Edwards, R. N., Garland, G. D., Kurtz, R. D. & Pitcher, D., 1974. *J. geomagn. geoelect.*, 26, 125–146.
Bailey, R. C. & Edwards, R. N., 1976. *Geophys. J. R. astr. Soc.*, 45, 97–104.
Banks, R. J., 1973. *Phys. Earth planet. Int.*, 7, 339–348.
Banks, R. J., 1975. *Geophys. J. R. astr. Soc.*, 43, 83–101.
Banks, R. J. & Ottey, P., 1974. *Geophys. J. R. astr. Soc.*, 36, 321–335.
Beamish, D., 1976. *PhD thesis, University of Lancaster.*
Dragert, H., 1973. *Can. J. Earth Sci.*, 10, 1089–1098.
Dyck, A. V. & Garland, G. D., 1969. *Can. J. Earth Sci.*, 6, 513–516.
Everett, J. E. & Hyndman, R. D., 1967. *Phys. Earth planet. Int.*, 1, 24–34.
Gough, D. I., 1973. *Geophys. J. R. astr. Soc.*, 35, 83–98.
Gough, D. I., Lilley, F. E. M. & McElhinny, M. W., 1972. *Nature Phys. Sci.*, 239, 88–91.
Gough, D. I., McElhinny, M. W. & Lilley, F. E. M., 1974. *Geophys. J. R. astr. Soc.*, 36, 345–362.
Jones, F. W. & Price, A. T., 1970. *Geophys. J. R. astr. Soc.*, 20, 317–334.
Lilley, F. E. M., 1974. *Phys. Earth planet. Int.*, 8, 310–316.
Lilley, F. E. M. & Bennett, D. J., 1972. *Geophys. J. R. astr. Soc.*, 29, 49–64.
Matsushita, S., 1967. *Physics of geomagnetic phenomena*, p. 301–424, eds S. Matsushita & W. H. Cambell, Academic Press, New York.
Parkinson, W. D., 1959. *Geophys. J. R. astr. Soc.*, 2, 1–14.
Porath, H., Oldenburg, D. W. & Gough, D. I., 1970. *Geophys. J. R. astr. Soc.*, 19, 237–260.
Price, A. T., 1949. *Q. J. Mech. appl. Math.*, 2, 283–310.
Schmucker, U., 1970. *Bull. Scipps Inst. Oceanography*, 13.